

Three-dimensional vortex dynamics in superfluid ^4He : Line-line and line-boundary interactions

K. W. Schwarz

IBM Thomas J. Watson Research Center, Yorktown Heights, New York 10598

(Received 21 December 1984)

The dynamical behavior of arbitrarily configured, interacting quantized vortex filaments is investigated by means of numerical experiments and analytical estimates. Several prototype situations of interest in the theory of superfluid turbulence and critical velocities are considered. It is shown that if a vortex loop approaches a surface to within a critical distance, a localized cusplike deformation is generated which drives the vortex into the surface at a well-defined point. If the vortex is reconnected to the surface in this limit, the two ends which now terminate on the surface quickly move apart. The entire process can be well approximated by making a simple reconnection at the critical distance. A similar process is found to occur when two vortex filaments try to cross, with two cusps developing which bring the lines together at a point in such a way that a line-line reconnection naturally ensues. More complicated versions of the reconnection process occur when a vortex terminates on a flat surface which contains a pinning site in the form of a local protrusion. Such a vortex is captured by the pinning site when it approaches to within a critical distance. Once a vortex is pinned, it requires a finite flow velocity to free it from the pinning site. At the depinning velocity, the vortex reconnects to the flat surface and moves off. An analytical depinning criterion involving both normal and superfluid velocities is derived, and found to be in good agreement with the numerical experiments.

I. INTRODUCTION

The appearance of quantized vortex lines in superfluid ^4He leads to hydrodynamic phenomena considerably more complicated and interesting than the simple potential flow considered in the Landau two-fluid model. Beginning with the work of Feynman,¹ the phenomenological description of quantized vortices as classical vortex filaments subject to an effective frictional force has become highly developed. This phenomenology has led to physically transparent and quantitatively accurate treatments of vortex arrays in the rotating superfluid²⁻⁷ and of quantized vortex rings.^{8,9} It is noteworthy, however, that many of the most fascinating phenomena involving quantized vortex lines have remained poorly understood. In the case of channel flow, for example, it is known that there exists a critical velocity above which the superfluid enters a turbulent state consisting of a dense, random tangle of quantized vortices.¹⁰ It has not been understood how these singularities are generated, or what determines the critical velocity. Similarly, it is not known how the rectilinear vortex arrays found in rotating helium are established. Many other phenomena, such as vortex pinning and the trapping and release of ions by vortices also raise interesting questions. Some progress has been made on a few of these problems, e.g., fully developed superfluid turbulence,^{11,12} thermally activated dissipation near the λ point,¹³ and ion trapping,¹⁴ but even here, basic questions remain unanswered.

Considering that literally hundreds of experimental studies have been published on these and related phenomena, the lack of substantial theoretical development which characterizes this field is surprising. It seems, in fact, natural to extend the vortex filament phenomenology

which has been so successful in dealing with geometrically simpler situations to these more complicated problems for which the three-dimensional dynamics of interacting quantized vortices plays the central role. The present paper initiates a systematic approach along these lines. First, the proper method of determining the three-dimensional motion of quantized vortex filaments is reviewed. It will turn out that this motion can be broken up into a locally induced part which depends only on the instantaneous local configuration of the vortex line, and a nonlocal correction which is often small. Exceptional configurations can develop in which a vortex filament approaches a boundary or another vortex very closely, and nonlocal terms suddenly become very important. Detailed calculations are presented which make it plausible to assume that such situations result in the essentially instantaneous reconnection of the line to the boundary or to the other vortex. In this way, one obtains a greatly simplified, yet still quite accurate, model which embodies the entire hydrodynamic problem in the dynamics of one or more three-dimensional topological line defects. The rules of the game are then elementary: The motion of a particular point on a line depends only on the shape of the line at that point; and interactions between lines or between a line and a boundary occur only when a very close approach takes place and a reconnection is made. Once this basic intuitive picture has been absorbed, it can be embellished in various ways.

It will be shown in this and subsequent papers that our approach is useful on several levels. The identification of topology-changing reconnections as a crucial feature of the line dynamics makes it possible to develop plausible qualitative explanations of the various phenomena mentioned above. Rigorous dimensional analysis of the refor-

mulated problem is sometimes possible, and yields an explanation of many observed functional dependences. Finally, the line-singularity description can be used as a basis for developing analytical models, or it can be embodied in numerical simulations to yield quantitative predictions which can be compared with experiment. The emphasis in this series of papers will be on the computational approach, which makes up in power what it lacks in elegance.

As an initial application of our approach, various aspects of the vortex pinning problem will be investigated. Preliminary reports on some of these results have appeared previously.¹⁵⁻¹⁷ Other problems will be treated in subsequent papers.

The numerical codes that have been developed to work out the implications of the theoretical ideas reproduce the fully nonlocal, three-dimensional motion of arbitrarily configured vortex filaments. In the calculations discussed here, a frictional force acting on the vortex core is always included. Aside from being appropriate to the superfluid ⁴He situation, such a term has a salutary effect on the stability of our numerical algorithms. It is to be noted that this frictional force represents a classical dissipative mechanism quite different from, and in fact much simpler than, the viscosity of an ordinary fluid. In the long run, therefore, vortex filaments in the superfluid have a different fate from those in a classical fluid. In the short run, however, and as long as the core structure of the vortex filaments does not become an issue, they behave identically. Thus, a number of our results are directly relevant to classical fluid dynamics where the subject of three-dimensional interacting vortex filaments is of considerable current interest. Indeed, in a recent paper devoted to this topic, Siggia¹⁸ has also identified the collapse to a point of two interacting lines which is discussed in Sec. III B. Interestingly, his idea of what happens at the end of such a collapse differs from ours. On this level there may very well be profound differences between quantized and classical vortices.

II. MOTION OF A QUANTIZED VORTEX LINE

A vortex filament can be constructed by defining a thin core passing through the fluid (Fig. 1), and requiring the fluid velocity $\mathbf{v}(\mathbf{r})$ outside the core to have zero curl and divergence, while the line integral $\kappa = \oint \mathbf{v} \cdot d\mathbf{l}$ around the core is assumed to have some nonzero value. It is predicted theoretically and observed experimentally that vortex filaments with the particular value $\kappa = h/m_4$ can occur in superfluid helium, where h is Planck's constant and m_4 is the mass of the helium atom. The core radius a_0 of these quantized vortices is found experimentally to be of order 10^{-8} cm. Outside this core region, the superfluid velocity field \mathbf{v}_s has a classically well-defined meaning, and can be described in terms of ideal fluid mechanics. At finite temperatures, the scattering of elementary excitations by the vortex will exert a frictional force \mathbf{f} per unit length on the fluid near the vortex core. The effect of this additional term can also be incorporated into a simple vortex-filament formalism. On this level, the quantities κ , a_0 , and \mathbf{f} appear as phenomenological parameters describing the

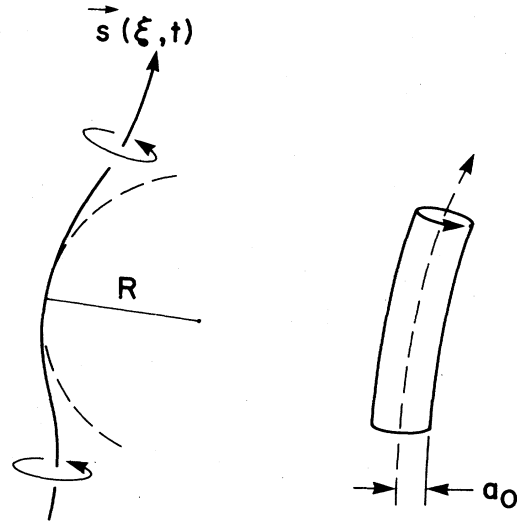


FIG. 1. Global and local views of a vortex filament.

properties of a classical vortex filament. Discussions of the underlying quantum-mechanical justifications of this model (such as they are) can be found in various review papers.¹⁹⁻²³ We shall be concerned with developing its large-scale implications.

Our attention will largely be confined to the limit where a_0 is small compared to other characteristic distances in the problem such as the radius of curvature R of the filament, or the distance between filaments. It is only in this limit that the details of the core structure cease to matter, and the procedure of treating quantized vortices as classical objects is justified. In this limit, too, vortex dynamics takes a relatively simple form^{24,25} which we shall now describe briefly in terms of its applicability to quantized vortices.

A. Vortex filament in an infinite fluid

If there are no extraneous forces acting on a vortex core, it must move with the fluid. Thus, the velocity field associated with the vortex filament acts back on the core itself to generate the motion of the filament in almost a purely kinematic way. The velocity produced at a point \mathbf{r} in the fluid by a vortex filament in the absence of boundaries is given by the familiar Biot-Savart expression:

$$\mathbf{v}_{s,\omega}(\mathbf{r},t) = \frac{\kappa}{4\pi} \int_{\mathcal{L}} \frac{(\mathbf{s}_1 - \mathbf{r}) \times d\mathbf{s}_1}{|\mathbf{s}_1 - \mathbf{r}|^3}, \quad (1)$$

where the curve described by the vortex line is specified in the parametric form $\mathbf{s} = \mathbf{s}(\xi, t)$ and \mathbf{s}_1 refers to a particular point on this curve. Equation (1) assumes that the vortex is infinitely thin, and only applies when $|\mathbf{s}_1 - \mathbf{r}| \gg a_0$. Thus, in attempting to determine the velocity at a particular point $\mathbf{r} = \mathbf{s}$ on the vortex, one finds that the integral diverges as $\mathbf{s}_1 \rightarrow \mathbf{s}$. Exactly how this divergence is healed by the finite core structure is a subtle and much-discussed problem in classical hydrodynamics. Furthermore, such discussions are not directly transferable to the case of quantized vortices where the physics of the core is quite

different. A simple expedient for dealing with this difficulty is to obtain the desired information experimentally. The first step is to note that the propagation velocity of a quantized vortex ring is observed to obey the expression for the velocity of a classical vortex ring,^{24,26}

$$\dot{\mathbf{s}}(\text{ring}) = \frac{\kappa}{4\pi} \frac{\hat{\mathbf{z}}}{R} \ln \left[\frac{8R}{e^{1/4} a_0} \right], \quad (2)$$

provided a_0 is treated as an adjustable parameter. Here, κ is the quantum of circulation, R is the radius of the ring, and $\hat{\mathbf{z}}$ is the normal to the plane of the ring. The value of a_0 is found to be about 1.3×10^{-8} cm, increasing slightly with increasing temperature.^{8,9} The second step is to consider a particular point \mathbf{s} on the ring (Fig. 2). The contribution to $\dot{\mathbf{s}}$ which arises from those parts of the ring for which $|\mathbf{s}_1 - \mathbf{s}| \gg a_0$ can be evaluated by carrying out the integral of Eq. (1) over the path indicated in Fig. 2:

$$\dot{\mathbf{s}}(\text{nonlocal}) = \frac{\kappa}{8\pi} \frac{\hat{\mathbf{z}}}{R} \ln \left[\cot\left(\frac{1}{4} |\phi_+|\right) \cot\left(\frac{1}{4} |\phi_-|\right) \right]. \quad (3)$$

Subtracting Eq. (3) from Eq. (2), and approximating $\tan(\phi/4)$ by $l/4R$, one obtains the local contribution arising from a curved-line element acting on itself,

$$\dot{\mathbf{s}}(\text{local}) = \frac{\kappa}{4\pi} \frac{\hat{\mathbf{z}}}{R} \ln \left[\frac{2(l_+ l_-)^{1/2}}{e^{1/4} a_0} \right]. \quad (4)$$

This applies to both quantum and classical vortices, with the difference that, for the former, a_0 must be interpreted as a quantum-mechanical cutoff parameter rather than a simple core radius.

Equation (4) provides the local contribution to the velo-

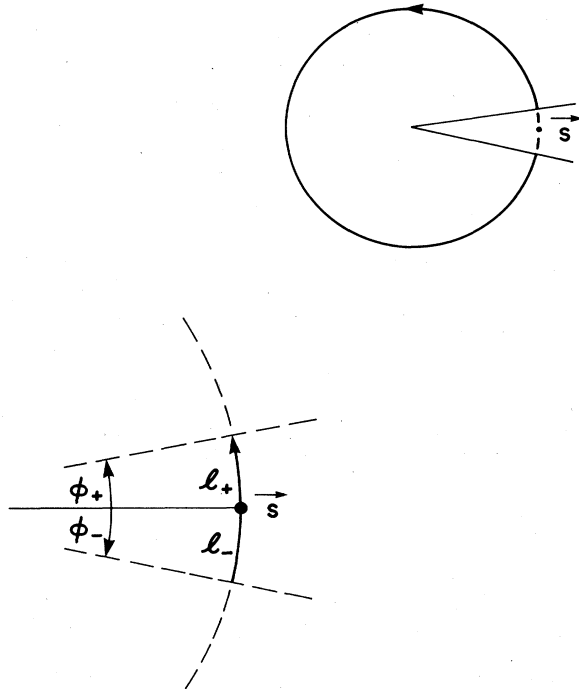


FIG. 2. Nonlocal (top) and local (bottom) contributors to the motion of the point \mathbf{s} . The division is purely formal, and neither part can exist by itself.

city of an arbitrarily curving vortex, provided that $R \gg l \gg a_0$. The nonlocal contribution is obtained by carrying out the integral of Eq. (1) over the rest of the filament and any other filaments which may be present. In order to express Eq. (4) in more generally useful form, we note that associated with any point on the curve $\mathbf{s}(\xi, t)$ there exists a triad of mutually perpendicular vectors \mathbf{s}' , \mathbf{s}'' , and $\mathbf{s}' \times \mathbf{s}''$ pointing along the tangent, the principal normal, and the binormal, respectively (Fig. 3). The prime denotes differentiation with respect to the instantaneous²⁷ arc length, ξ . The magnitudes of the vectors in the triad are 1, R^{-1} , and R^{-1} , respectively, where R is the local radius of curvature. The expression for the frictionless motion of a vortex filament in an unbounded fluid then becomes

$$\dot{\mathbf{s}} = \frac{\kappa}{4\pi} \mathbf{s}' \times \mathbf{s}'' \ln \left[\frac{2(l_+ l_-)^{1/2}}{e^{1/4} a_0} \right] + \frac{\kappa}{4\pi} \int_{\mathcal{L}} \frac{(\mathbf{s}_1 - \mathbf{s}) \times d\mathbf{s}_1}{|\mathbf{s}_1 - \mathbf{s}|^3}, \quad (5)$$

where the prime indicates that the local element is to be omitted from the integral.

B. Boundaries

If boundaries are present, Eq. (1) must be supplemented by an additional velocity field $\mathbf{v}_{s,b}$. This field is determined by solving $\nabla \cdot \mathbf{v}_{s,b}$, $\nabla \times \mathbf{v}_{s,b} = 0$ subject to the boundary condition

$$(\mathbf{v}_{s,b} + \mathbf{v}_{s,\omega}) \cdot \hat{\mathbf{n}} = 0, \quad (6)$$

reflecting the requirement of zero flow into the boundary.²⁸ For situations where $\mathbf{v}_{s,\omega}$ at the boundary is adequately represented by Eq. (1), the calculation of $\mathbf{v}_{s,b}$ is straightforward in principle although it may be difficult in practice. A particularly obvious and useful case is that of a plane surface, where $\mathbf{v}_{s,b}$ is just the field of an image vortex constructed by reflecting the filament into the plane and reversing its direction (Fig. 4).

Special consideration must be given to the situation illustrated in Fig. 5, where the vortex filament terminates on the boundary. Two problems arise here. The first is that Eq. (1) is correct only if the integral is taken over closed contours. This can be dealt with by continuing the filament into the surface in some way, taking the line integral of Eq. (1) over both the real and continued vortex. The boundary correction $\mathbf{v}_{s,b}$ must, of course, be determined from the $\mathbf{v}_{s,\omega}$ field generated by the entire vortex, and the apparent arbitrariness which arises in $\mathbf{v}_{s,\omega}$ because the vortex can be continued in various ways is removed

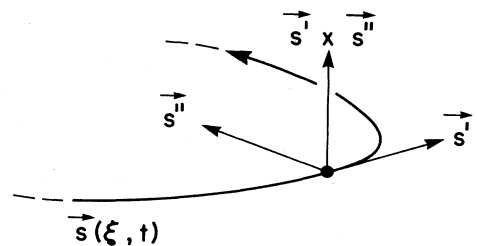


FIG. 3. Triad of vectors characterizing the instantaneous local configuration of the curve $\mathbf{s}(\xi, t)$.

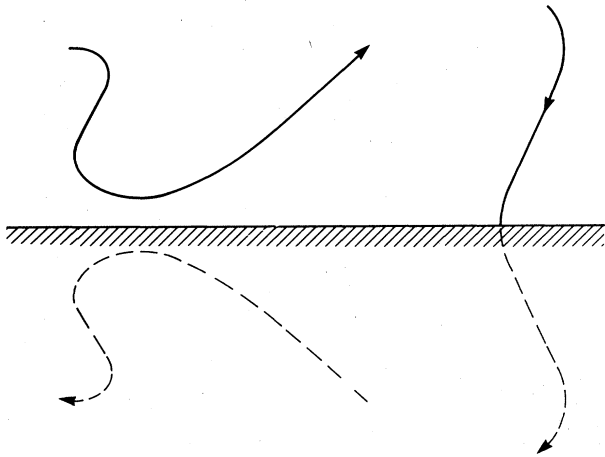


FIG. 4. Image vortices required to generate the boundary field $v_{s,b}$ of a plane surface.

when this $v_{s,b}$ is added. The second problem is that one must consider how to treat the divergence of Eq. (1) as $s_1 \rightarrow s_b$ when s_b is on the boundary. In order to keep things simple, it will be assumed that the surface curves only slowly on the scale of a_0 , from which it also follows that the filament enters the surface normally. The surface in the neighborhood of s_b can then be approximated as a plane, and the image construction shown in Fig. 5 suffices to determine the local contribution to \dot{s} at the special point s_b [i.e., it is obvious from symmetry that Eq. (4) applied to a local element constructed as in Fig. 5 takes care of both the divergent self-induced and the divergent boundary-induced contributions at s_b arising from the element itself. The effect of the rest of the vortex on s_b can be handled as before].

One final consequence of the presence of boundaries needs to be noted. If they are such as to make the fluid multiply connected, it becomes possible to specify addi-

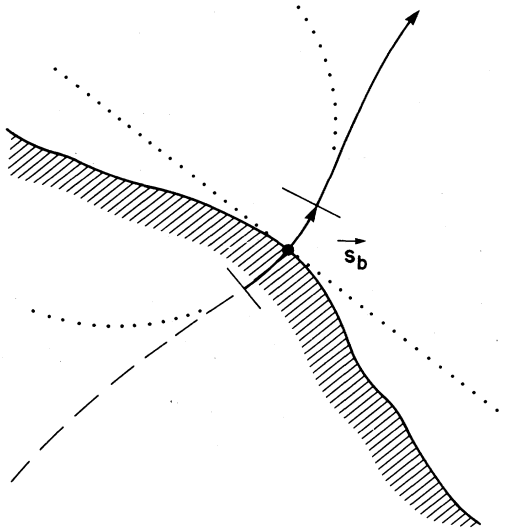


FIG. 5. Construction of the local element for a surface point s_b . Note that the velocity of s_b is always along the surface.

tional boundary conditions corresponding to additional flow fields. Common examples are flow through a tube or flow around an annulus. For want of a better word, such fields will be referred to as applied fields and denoted by $v_{s,a}$.

The total motion of the vortex filament is now described by

$$\dot{s}_0 = \frac{\kappa}{4\pi} s' \times s'' \ln \left[\frac{2(l_+ l_-)^{1/2}}{e^{1/4} a_0} \right] + \frac{\kappa}{4\pi} \int_{\mathcal{L}}' \frac{(s_1 - s) \times ds_1}{|s_1 - s|^3} + v_{s,b}(s) + v_{s,a}(s), \quad (7)$$

which is to be interpreted in the manner detailed above. In brief, the velocity of a given point s on the vortex will have a direct local contribution arising from the curvature of the element passing through s , a boundary correction arising from this element, a nonlocal contribution from real vortex elements not passing through s , a boundary correction to this nonlocal contribution, a nonlocal contribution due to vortex filaments continued into the boundaries, a boundary correction to this fictitious nonlocal contribution, and a term arising from any applied fields which may be present. Points where a vortex terminates on a boundary must be treated by use of the construction of Fig. 5, in which the first two terms of the above list combine to reproduce the result of Eq. (4).

C. Friction

A zero subscript has been added to the notation in Eq. (7) to denote the fact that it does not contain any dissipative effects. However, the elementary excitations of superfluid ^4He are strongly scattered by quantized vortices. Thus, if there is a net relative velocity between the gas of elementary excitations and the vortex, an "external" frictional force f per unit length will be exerted on the fluid in the neighborhood of the core. It can be shown from general momentum-conservation arguments applied to the fluid outside the core that such a force generates an additional motion of the vortex

$$\dot{s}_f = \frac{s' \times f}{\rho_s \kappa}, \quad (8)$$

which is such that the momentum flux due to the external force acting on the core region is transmitted out into the fluid as a reaction force. Since the normal excitation-gas fluid is assumed to respond independently from the superfluid field v_s , Eq. (8) does not contain the total density, but only the density $\rho_s = \rho - \rho_n$ which remains after the effective mass density of the normal fluid has been subtracted out.

Although f is not very well understood theoretically, it has been measured to a high degree of accuracy in experiments on rotating helium. The result, when expressed in our notation,²⁹ is

$$f / \kappa \rho_s = \alpha (v_n - \dot{s}_0)_\perp - \alpha' s' \times (v_n - \dot{s}_0), \quad (9)$$

leading at once to

$$\dot{s}_f = \alpha s' \times (v_n - \dot{s}_0) - \alpha' s' \times [s' \times (v_n - \dot{s}_0)], \quad (10)$$

where the second term on the right reflects the fact that the vortex is not a symmetrical scatterer, and it is assumed that there is no force acting parallel to the line. Here, the normal fluid velocity \mathbf{v}_n is the average drift velocity of the excitation gas.³⁰ Table I gives the temperature-dependent prefactors α and α' , which reflect the strength of the frictional interaction between the vortex core and the normal fluid.

It is important to note that $\dot{\mathbf{s}}_0$ in Eqs. (9) and (10) is not the actual velocity of the vortex, but the velocity [Eq. (7)] that the vortex would have in the absence of friction. Similarly, \mathbf{v}_n is not the velocity of the normal fluid in the neighborhood of the core, a quantity which is subject to vortex dragging effects, but rather the undisturbed velocity away from the core. As it happens, Eqs. (9) and (10) are precisely what is needed for our purposes, and the experimental values of α and α' can be utilized directly, without worrying about their microscopic interpretation. For further discussion of α and α' , as well as detailed references, the reader is referred to the recent review article of Barenghi, *et al.*²²

D. Qualitative considerations

The instantaneous motion of a given point on a quantized vortex is now given by

$$\dot{\mathbf{s}} = \dot{\mathbf{s}}_0 + \alpha \mathbf{s}' \times (\mathbf{v}_n - \dot{\mathbf{s}}_0) - \alpha' \mathbf{s}' \times [\mathbf{s}' \times (\mathbf{v}_n - \dot{\mathbf{s}}_0)], \quad (11)$$

where $\dot{\mathbf{s}}_0$ is calculated from Eq. (7). Although this description is an idealization which, for example, neglects the thermal fluctuations of the quantized vortices, it represents a well-tested phenomenology which it has long been believed gives an adequate description of the dynamics of quantized vortices. Equations (7) and (11) being nonlocal and nonlinear, their brute force application to arbitrarily configured, multiple vortices in the presence of nontrivial boundaries leads to excessive complications which only hide the interesting physics. Fortunately, Eqs. (7) and (11) are amenable to a number of straightforward approximations which lead to great simplifications at a very modest cost in accuracy.

The most important point to note is that, with rare exceptions, the local term in Eq. (7) completely dominates

the nonlocal term and the boundary corrections. The local term is of order $(\kappa/4\pi R) \ln(R/a_0)$, R being the radius of curvature at the point in question, while the nonlocal and boundary corrections are of order $\kappa/2\pi\Delta$, where Δ is some characteristic distance such as the distance to the nearest other line, or the distance to the nearest boundary. Consequently, the ratio of the local to nonlocal terms in Eq. (7) is

$$\frac{\text{local}}{\text{nonlocal}} \sim \frac{\Delta}{R} \ln(R/a_0). \quad (12)$$

Since a_0 is of microscopic dimensions, $\ln(R/a_0)$ is characteristically of order 10. Provided that $\Delta \gtrsim R$, it then follows that, to an accuracy of order 90%, Eq. (7) can be replaced by

$$\dot{\mathbf{s}}_0 = \beta \mathbf{s}' \times \mathbf{s}'' + \mathbf{v}_{s,a}, \quad (13)$$

where

$$\beta = \frac{\kappa}{4\pi} \ln \left[\frac{c \langle R \rangle}{a_0} \right], \quad (14)$$

with c a constant of order 1. In the expression for β , $(l_+ l_-)^{1/2}$ has been replaced by R , a procedure which takes some account of nonlocal corrections from nearby parts of the line. Since it affects the logarithm only marginally, R can further be replaced by its characteristic value $\langle R \rangle$ to make β a constant.

Equation (13) is known as the localized induction approximation in classical fluid dynamics,^{31,32} although we shall refer to it simply as the local approximation. Its 90% accuracy sets the standard to which we shall in general aspire. The approximation fails only when Δ becomes very small, as occurs when lines try to cross each other, or when they approach a boundary closely. The interesting new physics which arises when this happens will be explored in Sec. III. In addition, the local approxima-

TABLE I. Friction coefficients.

| T (K) | α | α' |
|---------|----------|-----------|
| 1.0 | 0.006 | 0.003 |
| 1.1 | 0.012 | 0.006 |
| 1.2 | 0.023 | 0.011 |
| 1.3 | 0.036 | 0.014 |
| 1.4 | 0.052 | 0.017 |
| 1.5 | 0.073 | 0.018 |
| 1.6 | 0.098 | 0.016 |
| 1.7 | 0.127 | 0.012 |
| 1.8 | 0.161 | 0.008 |
| 1.9 | 0.21 | 0.009 |
| 2.0 | 0.29 | 0.011 |
| 2.05 | 0.36 | 0.003 |
| 2.10 | 0.50 | -0.030 |
| 2.15 | 1.09 | -0.27 |

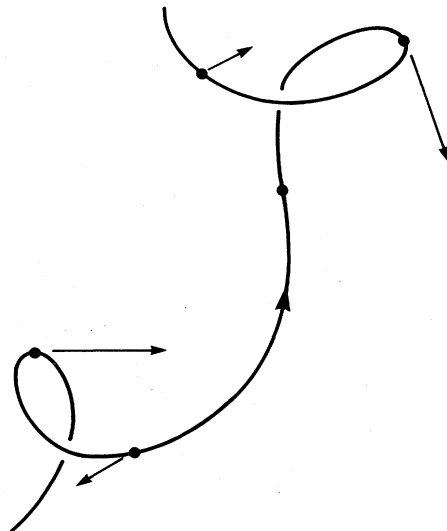


FIG. 6. Motion of a curving vortex. The lengths of the arrows reflects the speed with which the vortex filament is moving at that point.

tion becomes logarithmically less accurate as the scale of the problem is reduced [Eq. (12)], and becomes meaningless in the limit $\langle R \rangle \rightarrow a_0$. Equation (13), interpreted in the light of Fig. 3, readily lets one visualize the complicated motion experienced by a randomly curving vortex (Fig. 6), each point of which moves along the local binormal with a velocity inversely proportional to the local radius of curvature. It should be noted that we do not consider situations in which large numbers of vortices are preferentially oriented, thus giving rise to important nonlocal velocities extending over macroscopic distances. This, of course, is characteristic of rotating helium, where all of the vortices are aligned in the same direction. The extent to which vortex correlations play a role in other situations is not known. Presumably such effects could be incorporated into the formalism by interpreting $\mathbf{v}_{s,a}$ as a mean field which includes the averaged long-range effects of other vortices.

Turning now to the friction term, one notes that over much of the range of interest, α' is small compared to α . In any case, the α' term in Eq. (11) usually generates only a minor correction to $\dot{\mathbf{s}}_0$, and it is generally an excellent approximation to set $\alpha' = 0$. As an additional simplification, \mathbf{v}_n will here be treated as a specified, most often constant, field. In real life, of course, the frictional force acts back on the normal fluid and \mathbf{v}_n may need to be determined as part of the solution.

Since $\alpha \ll 1$ except near the λ point, the short-term vortex motion is usually only weakly affected by the friction. Nevertheless, the friction term is fundamentally important in that it gives rise to both growth and decay of vortex line length and in general plays the dual roles of driving force and dissipative mechanism.³³ One can readily see from Eq. (11) that if the normal-fluid wind blows sufficiently hard in the direction of the self-induced vortex velocity, the vortex will balloon out as in Fig. 7(a), leading to an increase in line length. If, on the other hand, the relative motion generates a normal-fluid headwind, the vortex will collapse inward as shown in Fig. 7(b), resulting in a loss of line. Writing out the equation of motion in the local approximation,

$$\dot{\mathbf{s}} = \beta \mathbf{s}' \times \mathbf{s}'' + \mathbf{v}_{s,a} + \alpha \mathbf{s}' \times (\mathbf{v}_n - \mathbf{v}_{s,a} - \beta \mathbf{s}' \times \mathbf{s}''), \quad (15)$$

one can, for a given value of the driving field $|\mathbf{v}_n - \mathbf{v}_{s,a}|$, identify a marginal radius of curvature

$$R_0 \sim \frac{\beta}{|\mathbf{v}_n - \mathbf{v}_{s,a}|}. \quad (16)$$

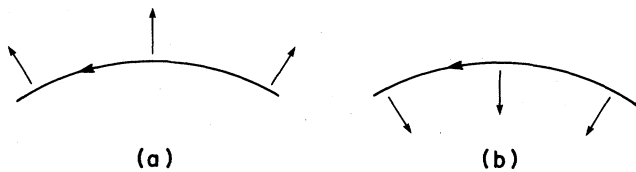


FIG. 7. Line gain and loss mechanisms. In (a) $\mathbf{v}_n - \mathbf{v}_{s,a} - \beta \mathbf{s}' \times \mathbf{s}''$ is pointing out of the plane of the figure, in (b) it is pointing into the plane.

If $R < R_0$, only line loss can occur, higher curvature regions such as kinks and bumps damping out preferentially. Regions for which $R > R_0$ can grow, provided the local binormal is properly oriented. Qualitatively, therefore, one has the picture of line length being pumped up at large scales and decaying away at the small scale end, somewhat analogous to a situation often found in classical fluids. Depending on the details of the problem, a vortex system subject to a driving field can disappear entirely, reach a stationary state where the vortices remain fixed, exhibit limit cycle behavior, or enter a topologically self-sustaining "turbulent" state.

III. RECONNECTION

The preceding section describes a complete procedure for determining the motion of quantized vortices. Subject to certain reasonable restrictions and approximations, arbitrarily complicated vortex configurations can be treated to any accuracy one pleases, or followed for any length of time desired. While the whole procedure of adding up the various contributions to the vortex motion at every point on the vortex is certainly a tedious one, it can easily be implemented numerically (see the Appendix). Once the relevant computer codes have been developed, numerical experiments can be performed which make previously obscure situations transparently clear. The insights developed from such studies often suggest simplifying approximations which permit one to attack still more complicated problems, or which can serve as the basis for the development of analytical models. It is with this aim that we now investigate the question which was left unresolved in the preceding section, namely, how to deal with those exceptional situations where filaments try to cross each other or to approach a boundary, and the nonlocal corrections suddenly become very important. All calculations in this section were carried out using the full nonlocal dynamics of Eqs. (7) and (11). The friction coefficients were typically set at $\alpha = 0.10$ and $\alpha' = 0$. Further discussion is given in the Appendix.

A. Interaction of a vortex line with a plane

Many of the features we wish to isolate can be deduced by looking at the simple case of a vortex loop interacting with a plane boundary. The qualitative expectation is that the image field will act most strongly on that part of the loop nearest the boundary, retarding it as in Fig. 8. The self-induced motion of this part of the loop now develops a component into the boundary, causing the loop to approach more closely and increasing the image effect. A runaway phenomenon thus develops, connecting the loop to the boundary in an irreversible fashion.³⁴

In general, the boundary-generated field will compete with other sources of vortex motion in determining the fate of the vortex loop. If, for example, the loop in Fig. 8 is aimed away from the surface, or is distorted in a way which makes it rotate away from the surface, the self-induced motion can prevail and carry the loop away be-

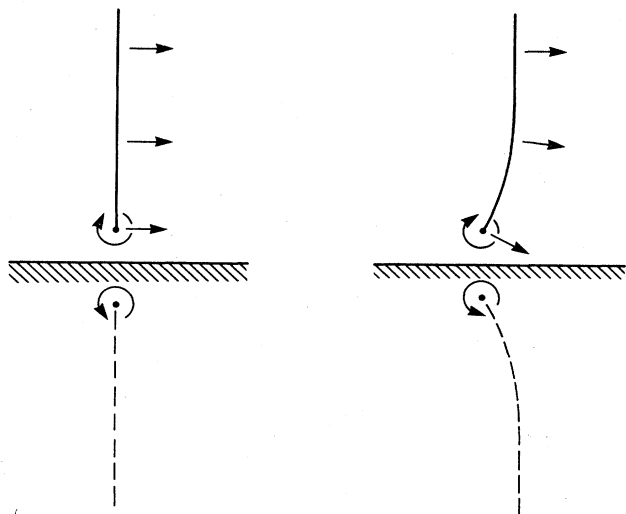


FIG. 8. Side view of a vortex ring travelling parallel to a plane boundary. The part nearest the surface is retarded by the boundary field.

fore it is trapped by the surface. Similarly, the loop may be shrinking because of friction with the normal fluid, and thus escape reconnection. Since, however, the image field increases in a highly nonlinear way as the loop ap-

proaches the boundary, it is possible to identify a characteristic critical distance Δ within which the image field becomes dominant and forces a reconnection. A crude estimate for Δ is obtained by asking how close the vortex loop has to approach before its boundary-induced motion becomes comparable to its self-induced motion. This leads to

$$\Delta \approx 2R / \ln(cR/a_0), \quad (17)$$

where, for consistency with later usage, Δ has been defined as the critical distance between the loop and its image. Confirmation of this estimate and, indeed, of the very usefulness of the critical-distance idea can be obtained by studying particular examples in detail. In this spirit, we consider the starting configuration shown in Fig. 9(a). This fourfold distorted ring is supposed to represent the case of a vortex which is randomly twisted over a length scale comparable to the average radius of curvature, a situation which characteristically arises in problems of interest to us. The motion of the bottom part of this loop in the absence of boundary effects is shown in Fig. 9(b). If the initial loop position is moved in close to the boundary, this behavior is modified only slightly [Fig. 9(c)]. Even a small further decrease of the distance between the loop and the boundary, however, leads to an entirely different development [Fig. 9(d)], which by now can be recognized as a reconnection event. It is clear not only that there is a well-defined critical distance inside of which the boundary traps the vortex, but also that a vortex loop outside this distance is only weakly affected by the boundary.

Values of Δ computed with this particular configuration for various scales are plotted as triangles in Fig. 10. They are seen to be in reasonable agreement with Eq. (17).

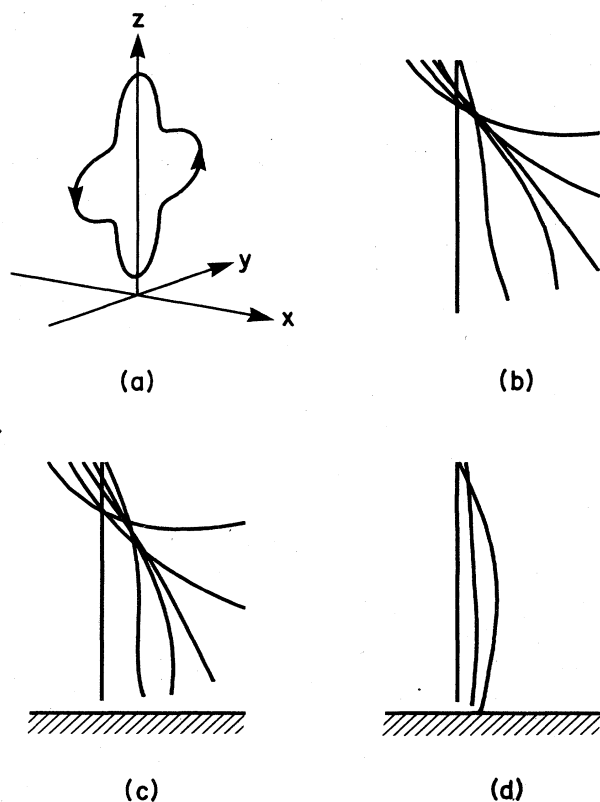


FIG. 9. Dynamics of a four-lobed loop near a surface. A perspective view of the initial configuration is shown in (a); (b)–(d) show side views looking along the y axis. Further information is provided in the text.

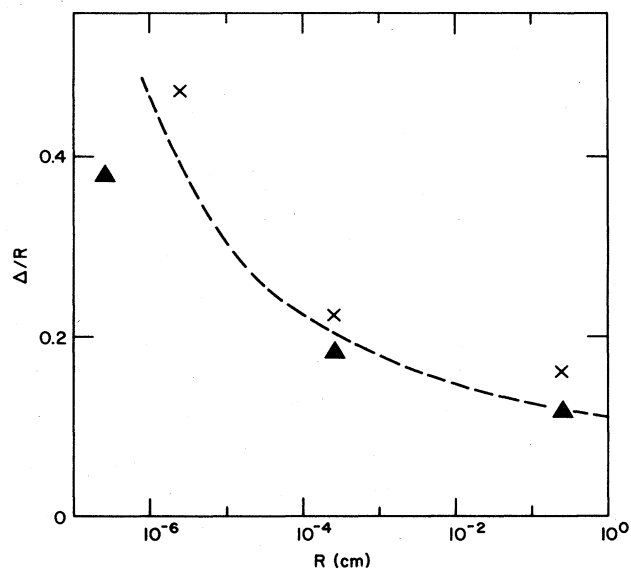


FIG. 10. Critical distance at which reconnection is initiated as a function of scale. Triangles, interaction of a four-lobed loop with a plane boundary; circles, line-line crossings. Other numerical studies yield equivalent results. The dashed line represents the prediction of Eq. (17).

Different configurations and conditions will of course yield somewhat different values of Δ , as the other example plotted in Fig. 10 shows. What is important to note, however, is that Δ is generally considerably smaller than the other characteristic dimensions in the problem. The general viewpoint one needs to cultivate, therefore, is that quantized vortex motion is practically unaffected by the presence of boundaries until a vortex happens to approach a boundary very closely, in which case a reconnection occurs. The exact value of Δ is usually not very critical.

It is interesting to consider the fate of the vortex singularity once it becomes involved in a boundary-induced runaway. Detailed numerical studies, such as the one displayed in Fig. 11, show that in fact such an event generates only a mild pathology in the form of a small, localized cusp connecting the vortex loop to the surface. The explanation for this is that although the image field increasingly pulls the vortex loop along the boundary, the self-induced velocity into the boundary of the distorted loop grows even more rapidly. Hence, the vortex singularity impacts the boundary at a well-defined limiting point. References 15 and 34, where the loop is qualitatively pictured as running off to infinity along the surface, are in error on this issue, although none of the conclusions

reached there are affected.

The behavior demonstrated in Fig. 11 is generic: Except for the singular case of a vortex ring normally incident on a perfectly flat boundary, all vortex loops approaching the boundary sufficiently closely will develop a small cusp connecting them to the boundary. The cusp will be generated quickly compared to the overall motion of the vortex, and can often be thought of as occurring instantaneously when the vortex reaches the critical distance Δ .

The runaway process can be followed by explicit calculation down to dimensions on the order of the core radius. In Fig. 11, for example, it has been followed until the vortex is 3 Å from the surface.³⁵ At this level, the finite-core structure becomes important, and what happens next presumably involves quantum-mechanical issues or, in the classical case, computational problems, which cannot be satisfactorily treated at present. We now make the very plausible, but admittedly *ad hoc*, assumption that in this limit the vortex singularity reconnects to the surface in some reasonable manner as shown very schematically in Fig. 12. The reconnected vortex then undergoes a characteristic further development (Fig. 13) in which the two ends of the now reconnected vortex move apart, eliminating the runaway cusp in the process. The perspective view of Fig. 14 shows exactly how this happens: a helical distortion forms at the reconnection point and propagates outward. The whole process again happens rapidly, and from the point of view of the long term behavior of the vortex, the whole runaway, reconnection, and outward propagation process can be replaced by making a crude reconnection when the vortex first penetrates inside the critical distance Δ .

To sum up, a detailed examination of how a vortex loop interacts with a plane boundary leads to the conclusion that the vortex is practically unaffected by the presence of a boundary until some part of it comes within a distance $\sim R/\ln(cR/a_0)$ of the surface. When such a critical configuration occurs, the image field grabs the vortex and pulls out a small cusp connecting the vortex loop to the surface. It is assumed that when the vortex core touches the surface, the vortex switches over to terminate on the surface. The two ends of the singularity then move apart, and all the small scale details of how the reconnection was made become irrelevant. The end result is that the vortex singularity has undergone a discontinuous change in its topology. It is important to emphasize that although the ultimate switching of the singularity to the boundary is introduced *ex cathedra*, the formation of the reconnection cusp is a macroscopic phenomenon which can be calculated within the vortex-filament formalism. In this sense, the reconnection phenomenon arises as a feature of classi-

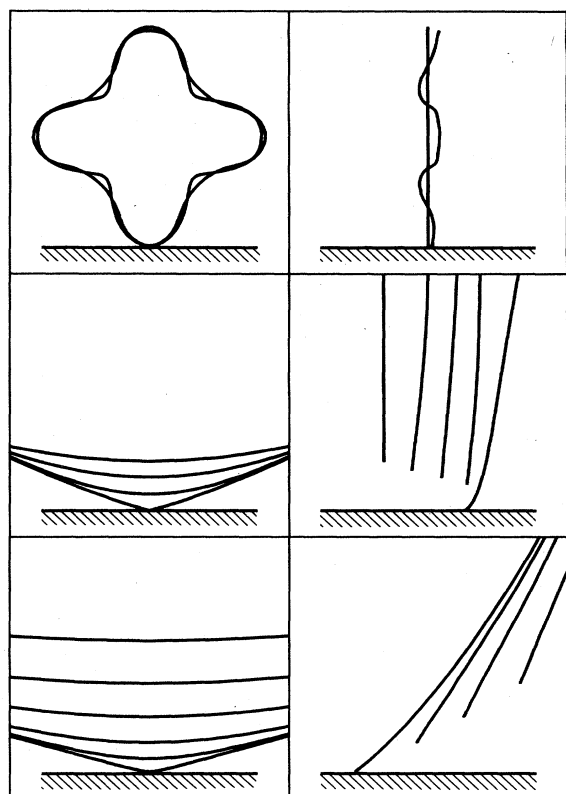


FIG. 11. Front and side views of a loop capture event. The top pair show the initial and final configuration of an initially planar four-lobed loop. The middle and bottom figures show the development of the cusp at a magnification of 25 and 625, respectively. The size of the loop is 2.5×10^{-3} cm and its initial distance from the plane is 3×10^{-5} cm. In the final configuration it has approached to within 3×10^{-8} cm.

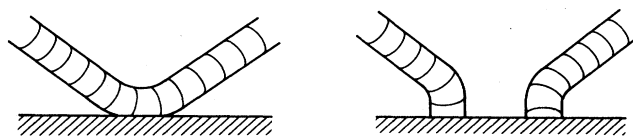


FIG. 12. Highly schematic view of what is assumed to happen when the core touches down.

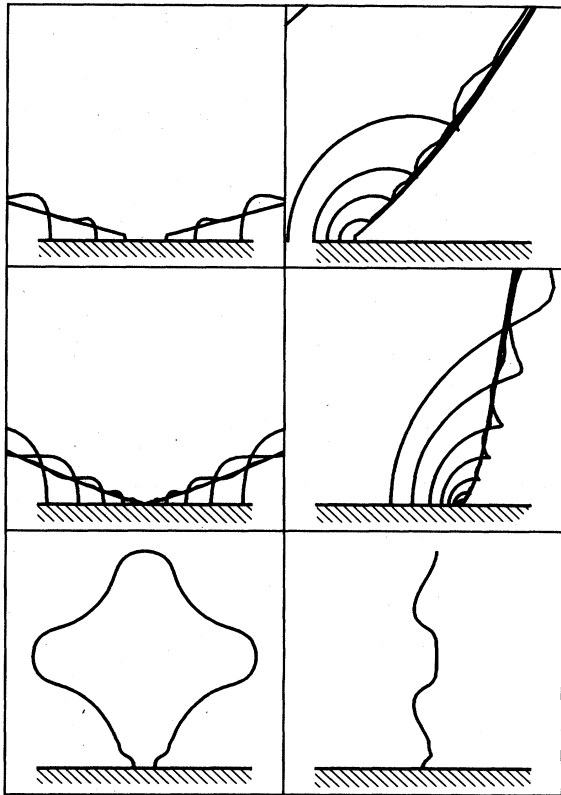


FIG. 13. Front and side views showing the separation of the two vortices after the microscopic reconnection has been made. The top and middle figures show the development at a magnification of 625 and 25 respectively. The bottom figures show the final configuration. The reconnection is made using the final configuration of Fig. 11.

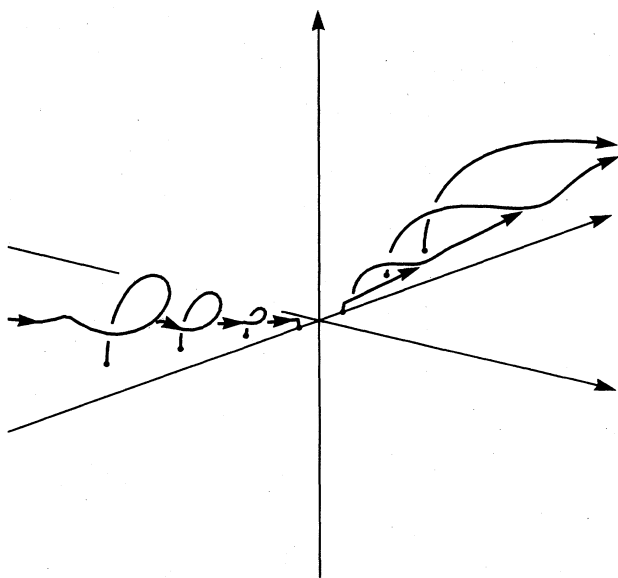


FIG. 14. Perspective view of the two ends moving apart in a solitonlike motion after the microscopic reconnection.

cal vortex-filament dynamics, and the conditions under which it occurs can be predicted.

B. Interaction of a vortex line with another line

In the typical three-dimensional vortex problem, the dynamics is dominated by the self-induced velocity discussed in Sec. II A, and is adequately described by the local approximation. It is clear, however, that this approximation breaks down when two filaments approach each other so closely that the nonlocal fields become important. A typical encounter (Fig. 15) will involve only a small segment of each line, and the characteristic distance for strong interaction will again be given by Eq. (17). We now ask exactly what happens in such an encounter.

The discussion of the preceding section already gives the answer for a particular case. If, for example, in Fig. 8, one promotes the image vortex to the status of a real vortex, eliminating the boundary, then the development of the two symmetrical vortices will be identical to that of the original vortex and its image. One can conclude that if two oppositely oriented vortex loops brush by each other sufficiently closely, a cusp connecting the two will develop, leading to a reconnection at the microscopic level, and a subsequent moving apart of the reconnected lines. In order to gain insight into the more general situation of Fig. 15 without becoming lost in an infinite number of special cases, the behavior of a vortex ring as it approaches an initially straight vortex line has been studied systematically. Figure 16 shows the initial configuration, the configuration of closest approach, and a subsequent configuration for various types of crossing attempts. The initial relative orientation between the two filaments as they encounter each other can be varied from 0° to 180° by varying the initial ring position, thus allowing one to investigate the characteristic behavior of vortex lines as they try to cross at various angles.

The top row of Fig. 16 is closely analogous to a surface

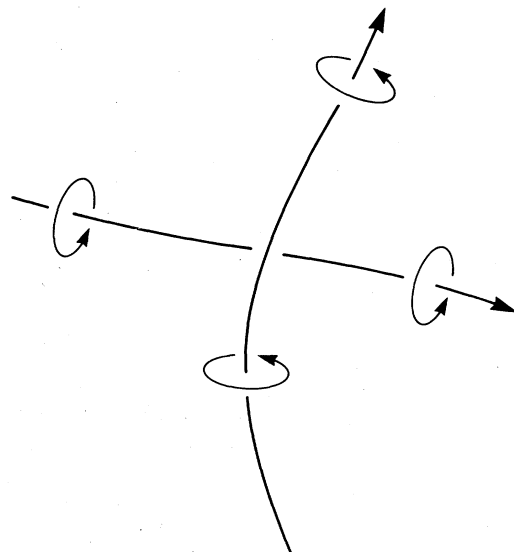


FIG. 15. Crossing encounter between two vortex filaments.

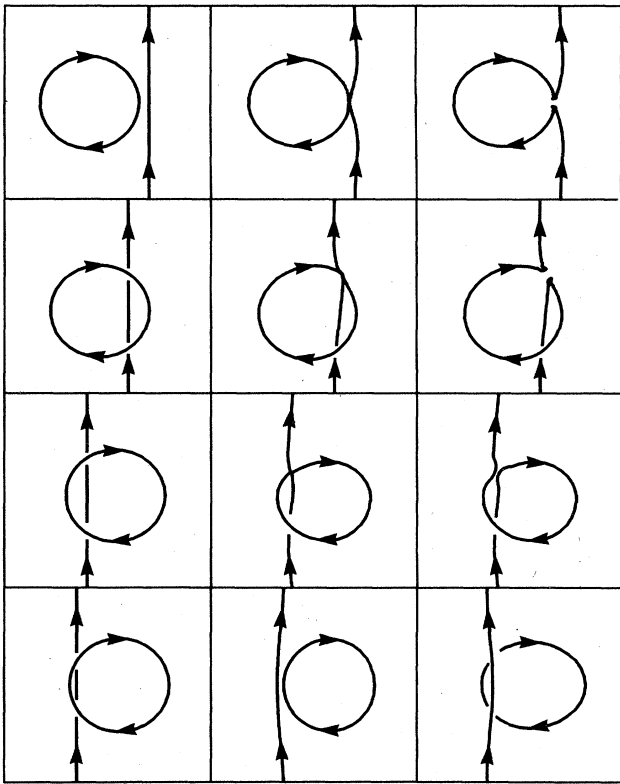


FIG. 16. Crossing encounters between a vortex ring and a line, viewed in the direction of ring propagation. Each row shows the initial configuration with the ring far away from the line, the configuration at the time of closest approach, and the state of the system some time after a microscopic reconnection has been made. The ring is tilted slightly so that the crossing takes place at one point on the line. The bottom row shows the only type of situation where a reconnection does not occur.

reconnection as just discussed. For the situation shown in the second row, where the interacting vortex elements approach each other in a more or less antiparallel orientation, the development is very similar. In both of these cases it is easy to see that the lines induce runaway distortions on each other, which cause them to join at a point (Fig. 17) in such a manner that their vorticity cancels in the neighborhood of this point. To obtain the subsequent development, we again assume that a reconnection occurs when the lines have approached to within an angstrom or so. As before, the result is a rapid separation of the reconnected loops (Fig. 18) arising from the high local curvatures generated by the reconnection.

The third row in Fig. 16 illustrates the more surprising fact that a similar reconnection will occur for practically any crossing angle. Even though the lines approaching each other are initially close to parallel, the distortions which they induce on each other cause them to twist around so that they become antiparallel at their closest point of approach. Figure 19 shows how this happens for two lines initially at right angles. Of course, once such a configuration has been achieved, the same kind of reconnection as before takes place.

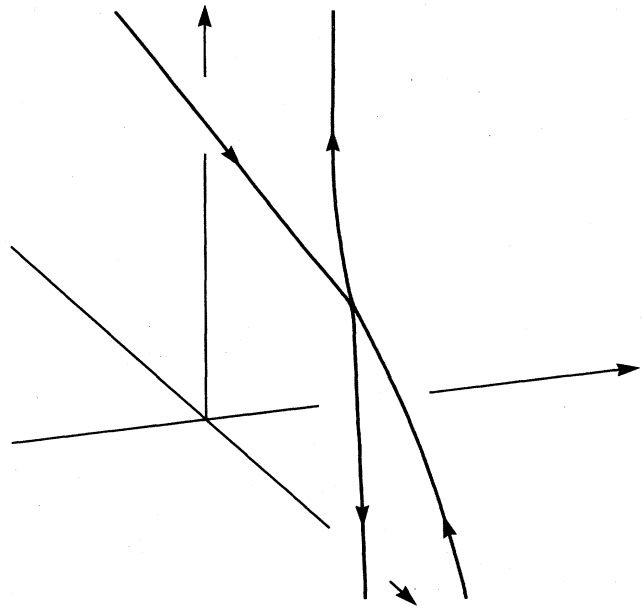


FIG. 17. Close-up perspective view of the line-line reconnection cusp for the situation illustrated in the second row of Fig. 16.

For the sake of completeness, one may note from the bottom row of Fig. 18 that there are special cases where lines can dodge around one another instead of reconnecting. Lines which are very close to being parallel can twist around each other several times before a cusp is formed. The conditions under which these kinds of things happen are quite atypical, and they are seldom important.

The result of these (and other) numerical studies lead to the conclusion that practically every case of an attempted

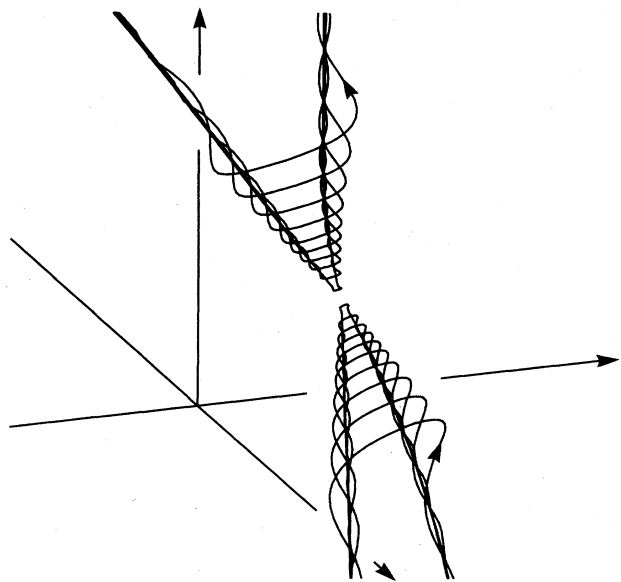


FIG. 18. Perspective view of the behavior after the lines of Fig. 17 are reconnected at the microscopic level.

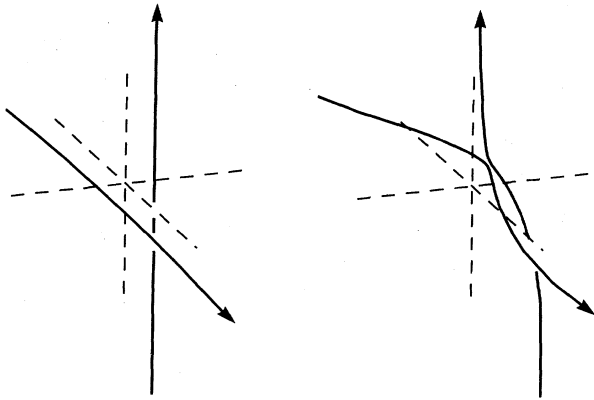


FIG. 19. Perspective view of two lines initially at right angles, reorienting each other to produce the reconnection cusp.

line-line crossing will lead to a topology-changing reconnection of the two lines. As in the case of the line-surface interaction studied in the preceding section, the motion of the lines is only weakly affected until a critical distance Δ is reached, at which stage the reconnection is initiated, entirely within the context of the hydrodynamic description. One sees in Fig. 10 that Δ deduced from the numerical line-line studies also agrees well with the estimate of Eq. (17). Again, it is plausible to assume that an actual reconnection occurs when the two lines have approached to within some microscopic distance such as the core size. Following the subsequent development, one finds that the final stage of the process looks very much as though a crude macroscopic reconnection had occurred at the distance Δ .

The cusplike instability of interacting vortex lines has also been found by Siggia¹⁸ in an independent investigation, and the reader is referred to Ref. 18 for a detailed analysis based on a somewhat different point of view.

C. Interaction of a vortex line with a sphere

The field $\mathbf{v}_{s,b}$ generated when a vortex is near a sphere can be written down analytically,³⁴ making this a suitable case for studying effects which arise when a vortex interacts with a nonplanar boundary. One of the most interesting of these is a vortex-capture phenomenon which is a complicated version of the process investigated in Sec. III A. The circumstances under which a vortex line will be captured by a sphere or equivalently by a hemispherical protrusion on a plane boundary (Fig. 20) are of interest in relation to the problem of ion trapping on vortex lines^{14,34} and the problem of vortex capture by a pinning site, respectively.

To find $\mathbf{v}_{s,b}$, the boundary value problem of Sec. II B is solved using the integrand of Eq. (1) as the source of a field $d\mathbf{v}_{\omega,b}$ arising from the element ds_1 . The resulting velocity potential is

$$d\Phi_{b,\text{out}} = \frac{\kappa}{4\pi} ds_1 \frac{b \sin\phi}{s_1 r} \sum_{n=1}^{\infty} \left[\frac{b^2}{s_1 r} \right]^n \frac{P_n^1(\cos\theta)}{n+1} \quad (18)$$

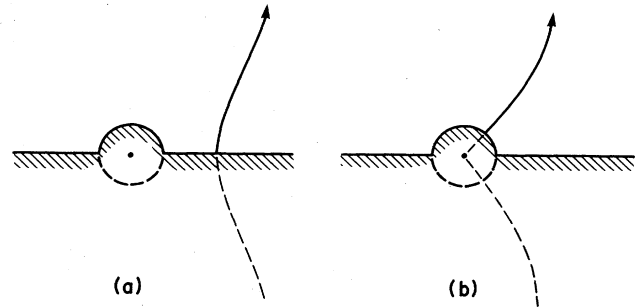


FIG. 20. Construction for treating a vortex interacting with a hemispherical pinning site. The problem is equivalent to that of a symmetrically extended vortex interacting with a sphere.

if the line element lies outside the sphere, and

$$d\Phi_{b,\text{in}} = \frac{\kappa}{4\pi} ds_1 \frac{\sin\phi}{r} \sum_{n=1}^{\infty} \left[\frac{s_1}{r} \right]^n \frac{P_n^1(\cos\theta)}{n+1} \quad (19)$$

if it lies inside the sphere. Here, P_n^1 are the associated Legendre polynomials, b is the radius of the sphere, and the various other quantities are defined in Fig. 21. The total boundary field³⁶ is obtained by summing over the entire vortex, including the dashed extensions shown in Fig. 20. The resulting $\mathbf{v}_{s,b}$ is then added to the bare vortex field and the applied field as in Eq. (7). A point terminating on the sphere, for which $\mathbf{v}_{s,\omega}$ and $\mathbf{v}_{s,b}$ are both divergent, must be treated according to the construction of Fig. 5.

In line with the central interests of the present paper, we shall concentrate on the pinning-site version of the capture problem. The specific case we choose to consider

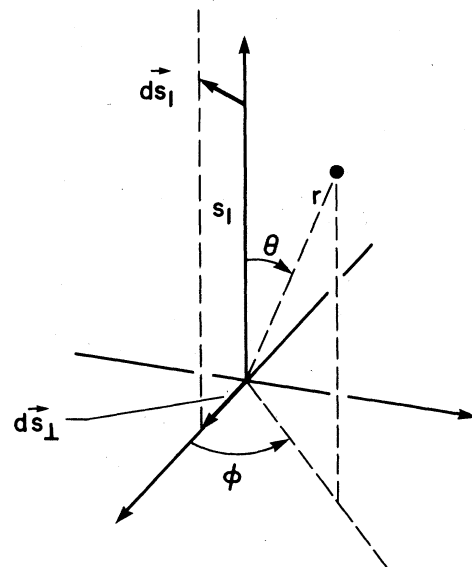


FIG. 21. Coordinate system for locating a point \mathbf{r} with respect to a particular line element ds_1 and the sphere. The origin is at the center of the sphere, the polar axis is determined by the position of ds_1 , and the azimuthal axis is the direction of ds_1 . Note that the axes change as one moves along the vortex.

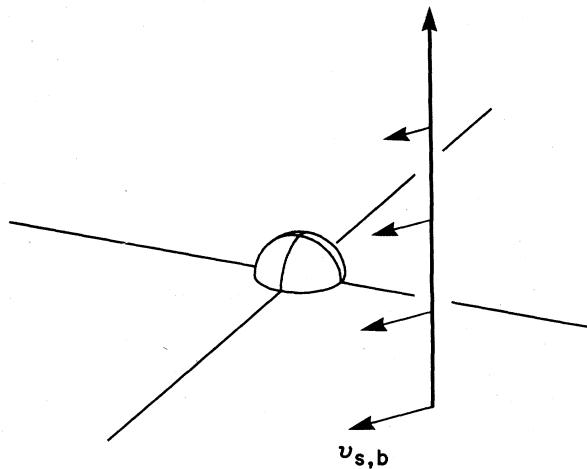


FIG. 22. Boundary field generated by the pinning site.

is a vortex extending between two smooth planes, one of which contains the pinning site. The boundary field tends to move the line around the sphere, this effect decreasing away from the sphere (Fig. 22). Again, it is clear that the boundary field acts to distort the line such as to generate a self-induced motion toward the sphere. The frictional component of the motion also causes the line to spiral in, and in fact becomes the main factor when the vortex is far away. In the absence of other disturbances to \dot{s} , an initially straight vortex will therefore undergo an elegant inward-spiralling motion (Fig. 23) which is one of the characteristic features of dissipative relaxation for quantized vortices. When the vortex gets close enough, a cusp is pulled out by the boundary field of the sphere, causing the vortex to approach the sphere infinitely closely at a well-defined point (Fig. 24). The qualitative similarity to the behavior studied in Sec. III A is clear, although the

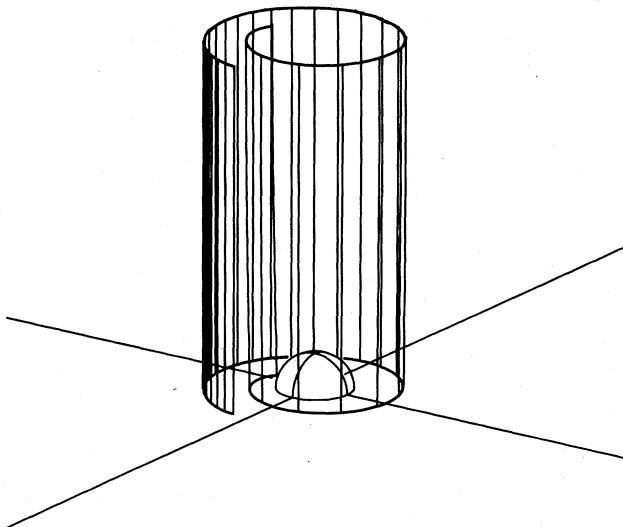


FIG. 23. Capture of a vortex in the absence of external disturbances. In this calculation, $b = 10^{-4}$ cm, the top plane (not shown) is at 10^{-3} cm, and $\alpha = 0.1$. Shown are sequential configurations of the vortex as it spirals in.

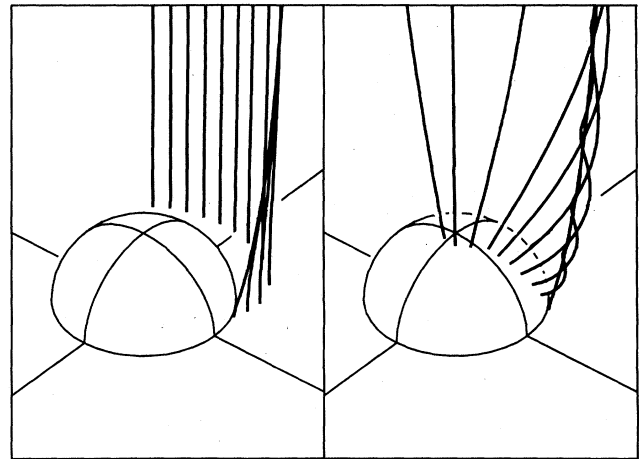


FIG. 24. Pinning reconnection and subsequent motion. Here $\alpha = 0.3$, to show the trapped vortex coming to equilibrium more quickly. Shown are sequential configurations of the vortex.

geometrical details are somewhat more complicated. As before, the only plausible assumption is that some kind of reconnection to the attracting boundary occurs as the vortex approaches the surface infinitely closely. The subsequent development (Fig. 24) obscures the details of this process and leaves the vortex attached to the pinning site.

If there are absolutely no disturbing effects, a vortex filament such as that shown in Fig. 23 will always be captured eventually. Competing sources of vortex motion

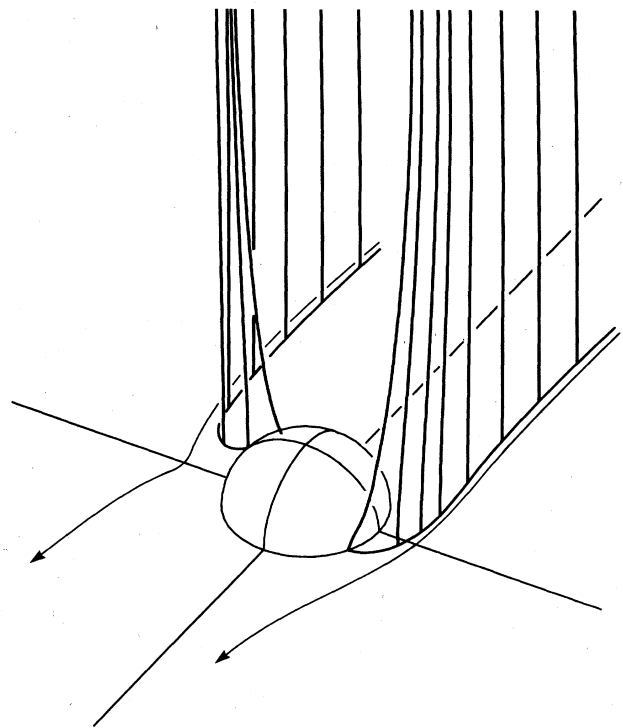


FIG. 25. Capture of moving vortices by a pinning site. Here $b = 10^{-4}$ cm, $D = 10^{-3}$ cm, $\alpha = 0.1$, and $v_{s,a} = 0.03$ cm s $^{-1}$. Paths of vortices starting slightly further out and avoiding capture are also shown.

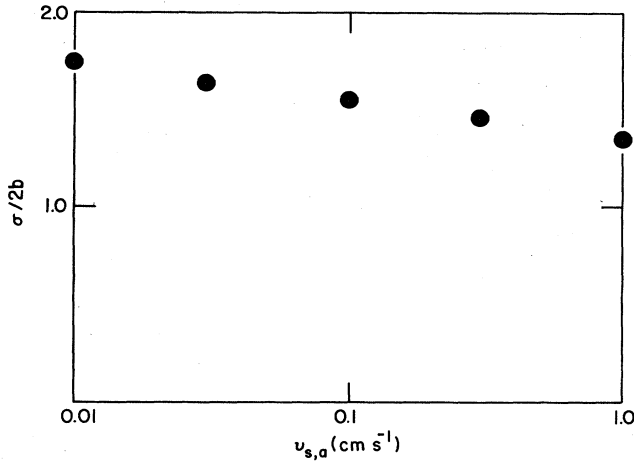


FIG. 26. Capture width of a hemispherical pinning site versus applied velocity. Here $b = 10^{-4}$, $D = 10^{-3}$ cm, $\alpha = 0.1$.

such as applied flow fields, velocities arising from neighboring vortices, or self-induced motion due to curvature in the filament, will, however, disrupt this capture process. Because the effect of the pinning site decreases rapidly with distance, even very small disturbances will drastically alter the behavior seen in Fig. 23. For any given situation, there will now be a specific region around the pinning site such that, if the vortex enters it, it will be captured. Otherwise, it will escape. Figure 25 illustrates the typical behavior when the vortex is swept towards the pinning site by an applied field.³⁷ Note that, although the magnitude of $v_{s,a}$ in this calculation is only $\frac{1}{30}$ of the characteristic velocity $(\kappa/4\pi D) \ln(D/a_0)$ of the problem, the view of Fig. 23 is already inappropriate. Rather, the vortex is now flushed past the pinning site by $v_{s,a}$ and will be captured only if it happens to pass sufficiently close so that the pinning site boundary field can grab it. Lines which pass by outside this critical distance are only weakly affected.

It is obvious from Fig. 25 that for the situation of a moving vortex, one can define an effective capture diameter σ . The typical variation of this quantity with $v_{s,a}$ is shown in Fig. 26. As one would expect, σ is only slightly larger than $2b$ at high velocities, and increases only very slowly as $v_{s,a}$ is reduced.

As always, the aim of our numerical calculations is to provide physical insight and suggest reasonable approximations. What one can conclude from the present section is that vortex filaments will be captured by localized protrusions through a reconnection process similar to that studied in Secs. III A and III B. A vortex moving past such a pinning site will be trapped if it passes within some critical distance of the site. Because the field generated by the protrusion is of short range, its effective capture width will at most be a few times its geometrical width, under experimentally realistic conditions. It should be noted that, although a hemisphere is probably a good prototype of the kind of pinning site which occurs in real life, the same approach can be used to investigate the effect of more gentle bumps or more extreme spikes. Such extensions are straightforward, and will be investigated only as necessary.

IV. PINNING

A vortex terminating on a plane boundary is free to wander about under the influence of its self-induced velocity as well as various applied and boundary-generated fields which may be present. In the preceding section, however, we saw that a protuberance can capture such a vortex. The boundary fields responsible for this process will in general act to keep the end of the vortex pinned to the protuberance even when quite large velocities are applied to the vortex. The occurrence of pinning in superfluid ⁴He has been appreciated on the phenomenological level for a long time and has been studied in several experiments.³⁸⁻⁴² Moreover, it has repeatedly been speculated that pinned vortices play an important role in the initiation of superfluid turbulence.^{1,19,43-45} Vortex pinning also arises in other areas, such as superfluid ³He, superconductivity, neutron-star physics, and classical hydrodynamics. The case of ⁴He, however, is by far the simplest since the interaction between the vortex and the pinning site is entirely determined by ideal fluid dynamics. Thus, the formalism developed above can be used to treat vortex pinning from a more fundamental point of view than is usually possible, i.e., as a dynamical consequence of the equations governing the superfluid velocity field.

A. Pinned vortex subject to pure superflow

What happens when a pinned vortex is subjected to an applied velocity $v_{s,a}$ tending to sweep it off its perch? We consider the geometry of Fig. 27, where the vortex extends between two symmetrically placed hemispheres of radius b protruding from planes spaced a distance D apart. In what follows, the origin is defined to lie at the center of the bottom pinning site, the \hat{z} axis is taken to run normally from the bottom to the top plane, and $v_{s,a}(\infty)$ is taken to point along the $+\hat{x}$ or $-\hat{x}$ direction. The applied field is assumed uniform far from the pinning sites, and takes the usual form for flow around a sphere²⁴ near the pinning site. For simplicity of comparison, many of the prototype calculations in this section have been done using the particular values $D = 2 \times 10^{-3}$ cm, $b = 10^{-4}$ cm, and

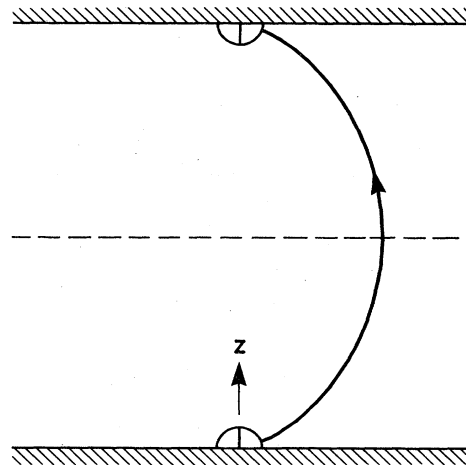


FIG. 27. Geometry for symmetrical pinning calculations.

$\alpha=0.10$, a relatively large pinning-site radius being chosen to make graphical display more convenient. The behavior obtained is, however, representative and changes in only relatively minor ways (which will be discussed) as these parameters are changed. Allowing for the obvious rescaling of distances, times, and velocities, a vortex in a 1-cm channel does not act very differently from a vortex in a 100-Å channel. If the initial vortex configuration has reflection symmetry about the center plane (dashed line), it will always maintain this symmetry, and the problem is then equivalent to a pinned vortex the upper end of which terminates on a smooth plane a distance $D/2$ away.⁴⁶ Figure 28 shows the development of such a vortex from an initially vertical position when a velocity field $v_{s,a}$ is applied. What one sees here illustrates the general fact that a pinned vortex of arbitrary initial configuration will spiral around in a complicated, often very elegant pattern until it comes to rest in a stationary configuration independent of initial conditions. The spiralling-in phenomenon arises from the action of the friction term, and as α is made larger, the vortex settles down more quickly.

Loosely speaking, the vortex remains pinned because any attempt of the line to move downstream in response to $v_{s,a}$ induces curvatures near the pinning site which cause the vortex to move around the pinning site. The resulting distortions propagate back up the vortex and, in partnership with the dissipative effect of α , generate the characteristic spiral motion seen in Fig. 28. It is to be emphasized that no supplemental constraints or "pinning forces" have been introduced into the formalism—the pinning phenomenon arises entirely within the context of the

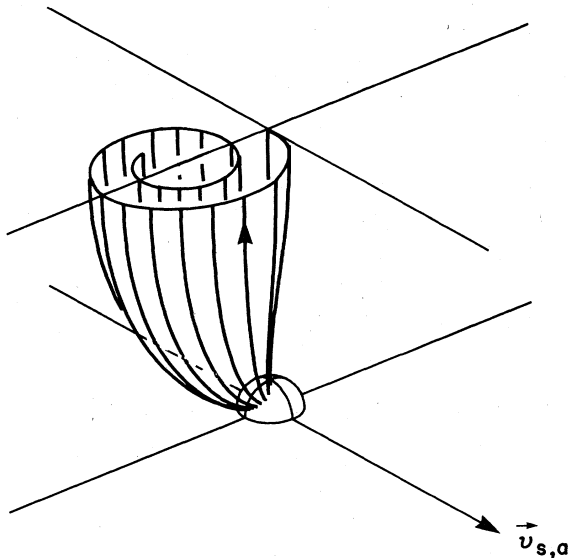


FIG. 28. Response of an initially straight pinned vortex to an applied velocity field. Here $D/2=1.0\times 10^{-3}$ cm, $b=1.0\times 10^{-4}$ cm, and $\alpha=0.10$. The applied field is $v_{s,a}(\infty)=0.50$ cm s⁻¹ in the direction shown, somewhat less than the critical velocity for depinning. Only the bottom half is shown.

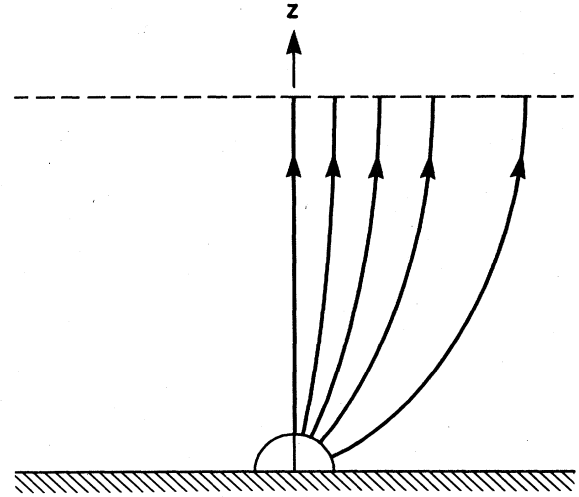


FIG. 29. Stationary configuration for various driving velocities. Here $D/2=1.0\times 10^{-3}$ cm, $b=1.0\times 10^{-4}$ cm. The values of $v_{s,a}(\infty)$ are 0.00, 0.17, 0.34, 0.51, and 0.68 cm s⁻¹ into the plane of the figure. Only the bottom half is shown.

ideal-fluid equation. To achieve its final, steady configuration, the vortex eventually adjusts itself to assume $\dot{\mathbf{s}}=0$ everywhere. It seems the most rewarding to the intuition to think of the vortex as adjusting its local curvature self-consistently so that its locally self-induced velocity exactly cancels out all the other contributions to $\dot{\mathbf{s}}$.

Given the symmetrical geometry of Fig. 27, the final configuration will lie entirely in the y - z plane bisecting the pinning sites, a situation in which all contributions to $\dot{\mathbf{s}}$ lie along the $\hat{\mathbf{x}}$ axis. Figure 29 shows how the stationary configuration varies with $v_{s,a}(\infty)$. As $v_{s,a}$ is increased, the vortex becomes more and more highly curved, in order for its self-induced velocity to cancel the applied velocity. Some additional curvature is required in the neighborhood of the pinning site because $v_{s,a}$ at the y - z bisector of the pinning site is greater than $v_{s,a}(\infty)$, and because the field of the image line becomes large near the boundary.

It is apparent from Fig. 29 that stationary configurations of this type do not exist at arbitrarily high driving velocities. Glaberson and Donnelly⁴³ have pointed out that if one ignores the complications which occur near the pinning site and treats $v_{s,a}$ as constant over the entire channel, then the vortex shape needed to provide a stationary configuration is just the arc of a vortex ring such that [see Eq. (2)]

$$v_{s,a} = \frac{\kappa}{4\pi R} \ln \left[\frac{8R}{e^{1/4} a_0} \right]. \quad (20)$$

It is not difficult to see that this works only for $R \gtrsim D/2$, implying a limiting applied velocity,

$$v_{s,\text{pin}} = \frac{\kappa}{2\pi D} \ln \left[\frac{4D}{e^{1/4} a_0} \right], \quad (21)$$

above which a stationary configuration is impossible. For channel shapes more complicated than the parallel-plate

geometry in Fig. 27, D should be interpreted as the smallest characteristic dimension across the channel. Obviously, a limitation similar to Eq. (21) must apply to our results. Actually, since the applied field is constant over virtually the entire channel, it may in fact seem that our results should be practically identical to those given by the argument of Ref. 43. Things, however, are not quite so simple, and the ability of the present approach to illuminate what is actually going on near the pinning site leads to a point of view which differs significantly from the heuristic considerations of Ref. 43.

As pointed out before, a stationary configuration requires a balance between the various contributions to \dot{s} . However, as $v_{s,a}(\infty)$ is increased, the vortex terminating on the sphere approaches the plane part of the boundary more and more closely and the image vortex begins to become important. The field of the image vortex can only be balanced out by an increase in the curvature of the vortex near the pinning site. Eventually, a critical distance is reached at which a balance can no longer be achieved, and the stationary configuration becomes dynamically unstable. The nature of the instability by now offers no surprises. Figure 29 was generated by increasing $v_{s,a}(\infty)$ in steps, waiting for the vortex to settle down to its stationary state each time. Upon passing through $v_{s,\text{pin}}$ (and the associated neutral-stability configuration), however, the image field suddenly achieves victory and pulls out a version of the by now familiar reconnection cusp (Fig. 30). In this version, the vortex approaches the plane boundary in a fashion which again makes it reasonable to suppose that a reconnection to the plane occurs when the core gets close. Again, such a reconnection leads to a rapid separation of the vortex from the pinning site (Fig. 31); and,

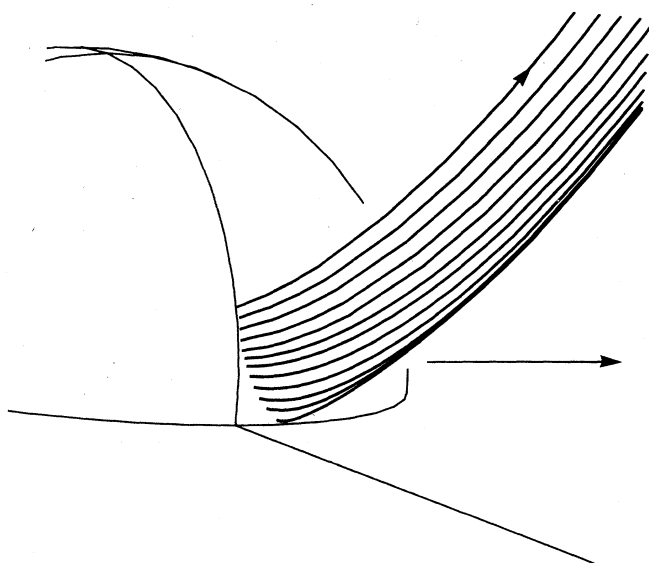


FIG. 30. Reconnection cusp pulled out by the image vortex when the critical depinning velocity is reached. The 0.68 cm s^{-1} stationary configuration of Fig. 29 becomes completely unstable when $v_{s,a}(\infty)$ is increased to 0.69 cm s^{-1} . The point terminating on the hemisphere moves into the surface, with the vortex parallel to the surface (antiparallel to its image) at contact. The flow direction is along the axis marked by an arrow.

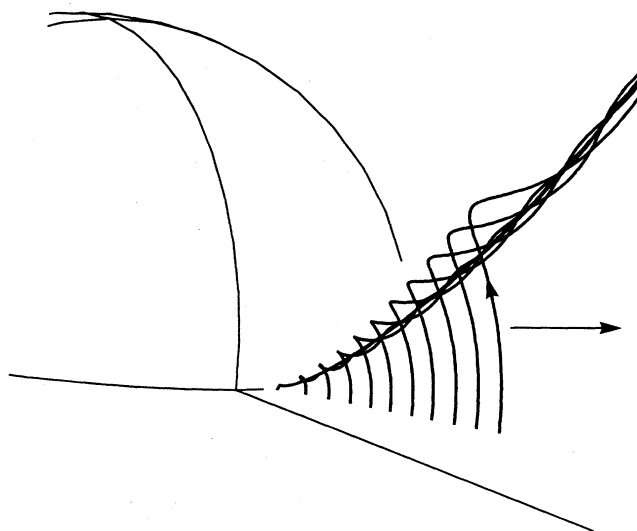


FIG. 31. Development of the vortex after a reconnection to the bottom plane has been established. The flow direction is along the axis marked by an arrow.

again, the net effect is as though a crude reconnection had occurred when the vortex line came within a critical distance of the plane boundary. More complicated pinning site geometries will lead to the same kind of behavior.

One concludes that beyond $v_{s,\text{pin}}$ the vortex undergoes a depinning reconnection to the plane—it jumps off the pinning site and is free to move away. This result may seem unsurprising from our present perspective, but it is at variance with the interpretation which up to now has been attached to $v_{s,\text{pin}}$, namely, that above $v_{s,\text{pin}}$, a single pinned vortex begins to act as a continuous source of vorticity. This speculation, which has repeatedly been advanced as an explanation for the onset of superfluid turbulence,^{1,43} is not supported by our work, nor is it in good agreement with experiment. While it appears quite likely that vortex pinning and depinning play an important role in determining the detailed phenomenology of the transition to turbulence in superfluid helium,⁴⁴ other mechanisms such as line-line and line-boundary reconnections are probably an equally important part of this very complicated process.

Accurate calculations of the vortex depinning velocity for the geometry of Fig. 27 have been performed as a function of b and D . The results, shown in Fig. 32, provide a useful standard against which more approximate calculations, analytical models, or analogous situations can be compared. It is found that $v_{s,\text{pin}}$ can lie significantly below the value predicted by Eq. (21), and that it decreases logarithmically with the size of the pinning site. The latter effect is due to the increasing relative importance of nonlocal effects as the scale of the problem is reduced: At smaller b , the vortex cannot come around so far on the pinning site before yielding to the image field. The variation of the critical configuration with b/D and with the overall scale reflects this fact, as illustrated in Figs. 33 and 34.

By analyzing the idealized case of Fig. 27, it is possible to develop a rather neat and useful approximate expres-

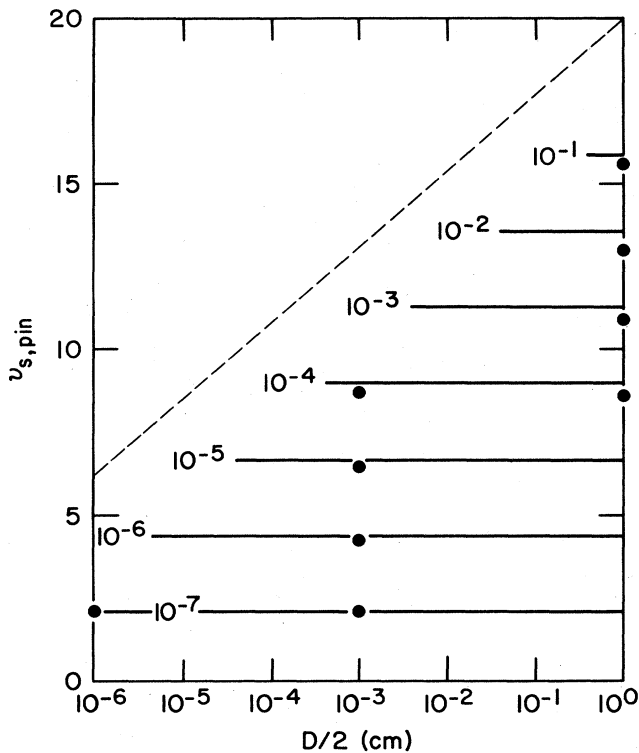


FIG. 32. The points show numerically calculated values of the critical depinning velocity in units of $\kappa/2\pi D$. The solid lines represent the predictions of Eq. (29) for various values of b in cm. The dashed line is the prediction of Eq. (21).

sion for the depinning velocity in pure superflow. In the absence of normal-fluid motion, stationarity requires $\dot{s}=0$. From Eq. (7),

$$\beta \frac{\partial \mathbf{s} / \partial \xi \times \partial^2 \mathbf{s} / \partial \xi^2}{|\partial \mathbf{s} / \partial \xi|^3} + \mathbf{v}_{s,b}(\xi) + \mathbf{v}_{s,a}(\xi) = 0, \quad (22)$$

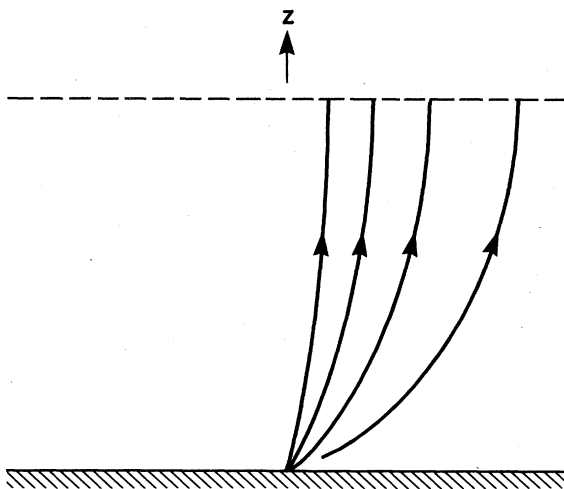


FIG. 33. Critical configurations for $D/2=10^{-3}$ cm, with b having values of 10^{-4} , 10^{-5} , 10^{-6} , and 10^{-7} cm, proceeding counterclockwise. The flow direction is into the plane of the figure.

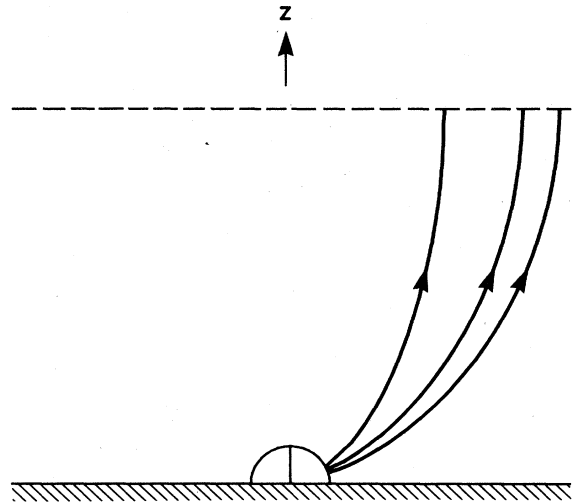


FIG. 34. Critical configurations for $2b/D=0.10$, with $D/2$ having values of 1, 10^{-3} , and 10^{-6} , proceeding counterclockwise. The flow direction is into the plane of the figure.

where position on the line is now denoted by a general parameter ξ not necessarily equal to the arc length. The effect of the line on itself is here being treated in the local approximation, so that β has the meaning of Eq. (14). The local approximation has, however, been refined in that the effect of the vortex extended into the boundary (Fig. 35) is explicitly included as $\mathbf{v}_{s,b}(\xi)$. Referring to the figure, it is clear that the part of the extended vortex running from 0 to A makes very little contribution to $\mathbf{v}_{s,b}$ while the part running from $-\infty$ to 0 contributes a field which tends to sweep the vortex off the pinning site in the same direction as $\mathbf{v}_{s,a}$, and which becomes large as θ_0 in-

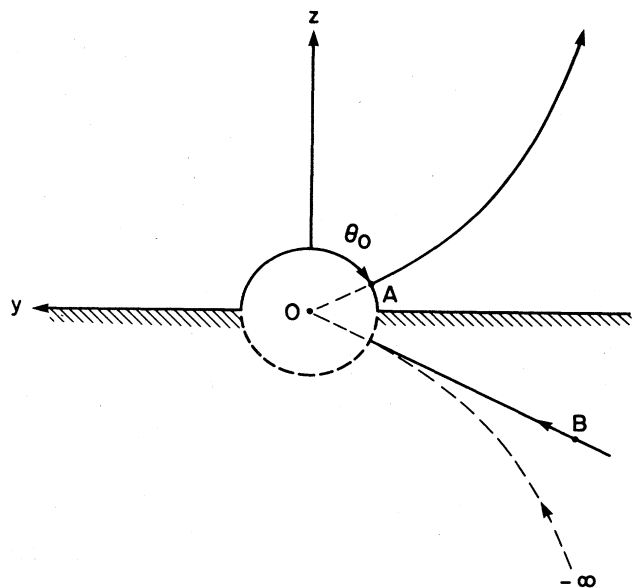


FIG. 35. Geometry for the calculation of the depinning velocity. The flow direction and the \hat{x} axis are into the plane of the figure.

creases. It is this term which causes the depinning instability.

If $v_{s,a}(\infty)$ is in the \hat{x} direction, as is assumed in Fig. 35, the stationary vortex lies in the y - z plane bisecting the sphere. It is then convenient to let $\xi=z$ and write

$$\mathbf{s}=(y(z), z), \quad (23)$$

$$\mathbf{v}_{s,b} + \mathbf{v}_{s,a} = v_s(z)\hat{x}. \quad (24)$$

A trivial integration then gives

$$\frac{y'}{(y'^2+1)^{1/2}} = -\sin\theta_0 + \beta^{-1} \int_{b \sin\theta_0}^z v_s(z') dz'. \quad (25)$$

That is, the y component of the tangent to \mathbf{s} starts at a negative value $-\sin\theta_0$ at a point $z=b \sin\theta_0$ on the sphere and increases, causing the vortex line to curve upward. The line must meet the $D/2$ symmetry plane vertically, i.e.,

$$\beta \sin\theta_0 = \int_{b \sin\theta_0}^{D/2} v_s(z) dz. \quad (26)$$

The trick now is to find a reasonable analytical approximation to $v_s(z)$. We write

$$v_s(z) = v_{s,a}(\infty) - \frac{\kappa \sin\theta_0}{4\pi z}. \quad (27)$$

The first term is just the applied flow field, ignoring the localized modifications due to the pinning site; the second is the field contributed by a straight vortex section which runs from $-\infty$ through B to 0 as shown in Fig. 35, and which we take to represent the dominant effect of the vortex extending from $-\infty$ to 0 in the figure. Equation (26) then integrates to give the condition on $\sin\theta_0$,

$$v_{s,a}(\infty) = \frac{\kappa \sin\theta_0}{2\pi D} \ln \left[\frac{b \cos\theta_0}{a_0} \right], \quad (28)$$

where we have set $\langle R \rangle = D/2$ in β , and have neglected b compared to $D/2$.

The maximum possible value of $v_{s,a}(\infty)$ in Eq. (28) can be identified as the depinning velocity. Curiously, as long as $b/a_0 \gg 1$, this occurs when both $\sin\theta_0$ and $\cos\theta_0$ are of order 1. For example, if $b/a_0=10$, $\sin\theta_0 \approx 0.80$, and $\cos\theta_0 \approx 0.60$. If $b/a_0=10^5$, the corresponding values are 0.95 and 0.31. Within the kind of accuracy we are shooting for, no significant additional error is then made by concluding

$$v_{s,\text{pin}} = \frac{\kappa}{2\pi D} \ln \left[\frac{b}{a_0} \right]. \quad (29)$$

This formula combines the three relevant size parameters in an appealingly simple way. Moreover, it gives an almost embarrassingly good fit to the numerical data, as illustrated in Fig. 32.

B. Effect of normal-fluid flow

The case of pure superflow considered in the preceding section illustrates most of the important features of the pinning phenomenon. Experimentally, however, \mathbf{v}_n is an independently adjustable field, forcing one to consider what additional features arise from its presence.

A problem to be faced immediately is what to take for $\mathbf{v}_n(\mathbf{r})$. Since the normal fluid behaves as a classical viscous fluid, it might be appropriate for the geometry of Fig. 27 to assume the usual parabolic flow profile

$$\mathbf{v}_n(z) = \frac{6\langle \mathbf{v}_n \rangle}{D^2} z(D-z), \quad (30)$$

with a suitable correction which makes $\mathbf{v}_n(\mathbf{r})$ go to zero on each pinning-site surface. On the other hand, the situation addressed in real life is more likely to be one where many other vortices are present,⁴¹⁻⁴⁵ in which case \mathbf{v}_n will be almost constant except very near the walls. Since this latter case is also more directly comparable to the considerations of the preceding section, we first consider what happens when \mathbf{v}_n is constant. The boundary conditions on each pinning site are satisfied heuristically by multiplying \mathbf{v}_n by the factor $1 - \exp[-(r-b)/b]$, where r is the distance from the center of the pinning site. It is granted that neither of these is strictly correct, but the vortex responds primarily to \mathbf{v}_n integrated across the whole channel. Hence, refinements such as making \mathbf{v}_n go to zero very near the walls or adopting a more realistic velocity variation near the pinning site have little effect.

Turning now to actual numerical experiments,⁴⁷ it is found that when a normal flow is applied ($v_{s,a}$ being kept at zero), an initially pinned vortex will spiral around in a manner analogous to that illustrated in Fig. 28, until it again reaches a stationary configuration. Such configurations are similar to those observed in pure superflow, except that the vortex no longer lies at right angles to the driving velocity (Fig. 36). Moreover, the stationary configuration now depends on the friction constant α as well as \mathbf{v}_n . Finally, it is found that the vortex actually no longer lies in an exact vertical plane, but deviates from this by a small amount.

An approximate analysis of Eq. (11) provides some illuminating insights. Assume that the vortex does indeed lie in a vertical plane, e.g., as in Fig. 27. Then \dot{s}_0 has no \hat{z} component, and Eq. (11) gives

$$\dot{s}_{0x} = \frac{\alpha^2 (s'_z)^2 v_n}{1 + \alpha^2 (s'_z)^2}, \quad (30a)$$

$$\dot{s}_{0y} = -\frac{\alpha s'_z v_n}{1 + \alpha^2 (s'_z)^2}, \quad (30b)$$

if \mathbf{v}_n is taken along the \hat{x} direction and $\alpha' = 0$. One would conclude from this that the plane described by the vortex lies at an angle $\phi = \tan^{-1}(\alpha s'_z)$ to the flow direction, and that whereas in pure superflow the vortex adjusts its configuration to balance out an applied motion $\mathbf{v}_{s,a} \approx v_{s,a}(\infty)$, in this case it adjusts itself to balance out an applied motion $\alpha s'_z v_n / [1 + (\alpha^2 s'_z)^2]^{1/2}$. In actual fact, of course, s'_z must change from 1 at $D/2$ to some lesser value as the vortex curves down to meet the pinning site. The resulting deviation from a planar configuration gives rise to a small \dot{s}_{0z} , leading to some further readjustments. The end result is essentially that of Eqs. (30), but with s'_z assigned an approximate effective value of 1. One therefore expects that \mathbf{v}_n will generate a vortex configuration similar to that generated by an effective superfluid velocity,

$$v_{s,a}(\text{eff}) \approx \alpha v_n / (1 + \alpha^2)^{1/2}, \quad (31)$$

but rotated so as to lie at an angle,

$$\phi \approx \tan^{-1} \alpha, \quad (32)$$

to the direction of \mathbf{v}_n . The argument is easily generalized to the case where the superfluid component is also flowing by adding $v_{s,a}^x$ to \dot{s}_{0x} and $v_{s,a}^y$ to \dot{s}_{0y} in Eqs. (30a) and (30b), respectively. It is to be emphasized that the above predictions again lie in the ubiquitous 10–20% error range. Figure 36 demonstrates, however, that once more a simple estimate works very well indeed.⁴⁸

Let us now for generality assume that both components are in motion, \mathbf{v}_n and $\mathbf{v}_{s,a}$ being colinear. When the neutrally stable configuration is reached, the vortex will, as before, reconnect to the plane and move off. Assuming that this happens when the corresponding $v_{s,a}(\text{eff})$ reaches the depinning velocity for pure superflow, one is led to a functional relation defining the depinning locus on the v_n , $v_{s,a}$ plane,

$$v_{s,\text{pin}} = \frac{\alpha^2 v_{n,\text{pin}} \pm [(1 + \alpha^2)^2 - \alpha^2 v_{n,\text{pin}}^2]^{1/2}}{1 + \alpha^2}, \quad (33)$$

where both $v_{s,\text{pin}}$ and $v_{n,\text{pin}}$ are expressed in units of $(\kappa/2\pi D) \ln(b/a_0)$. An example of such a depinning locus is shown in Fig. 37. If $\alpha \ll 1$, a condition which is realized not very far below the λ point, Eq. (33) approximates to the statement that $v_{s,\text{pin}}^2 + \alpha^2 v_{n,\text{pin}}^2 = 1$, in dimensionless units.

Equation (33) is very general, relating v_n , v_s , and α , as well as the geometrical constants. Although it is difficult to test its validity everywhere, some representative calculations have been performed. First, note that all of the

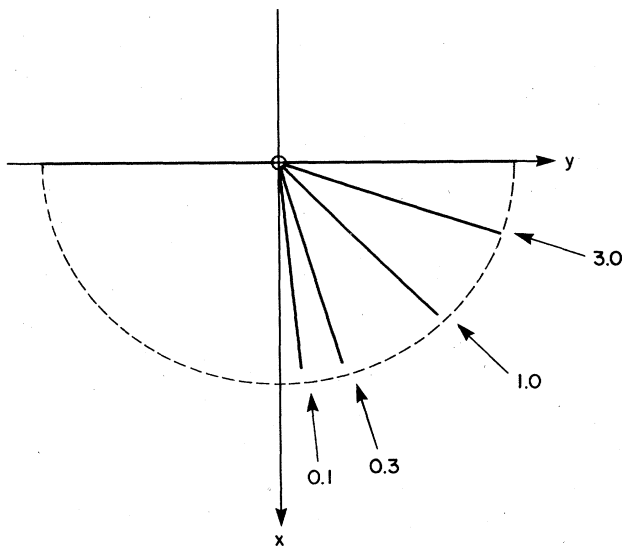


FIG. 36. Stationary vortex configurations (viewed from the top) for pure normal flow, with $D/2 = 1.0 \times 10^{-2}$ cm, $b = 1.0 \times 10^{-4}$ cm, and various values of α . The driving velocities v_n are adjusted to yield $v_{s,a}(\text{eff}) = 0.060$ cm s^{-1} . A simple rotation of the corresponding configuration for pure superflow yields the dashed circle. The indicator arrows show the angular position predicted by Eq. (32).

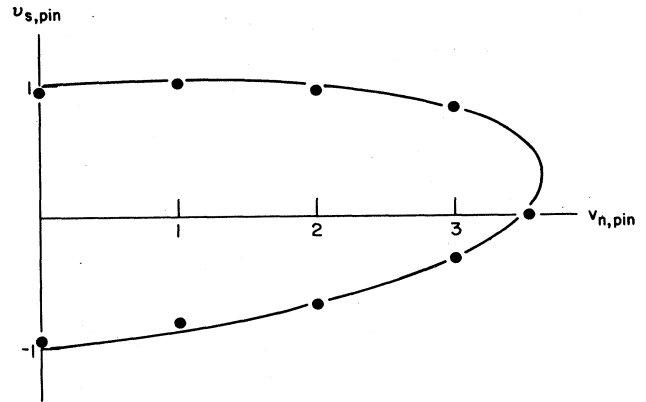


FIG. 37. The line is the depinning locus predicted by Eq. (33) for simultaneous normal and superflow, with $\alpha = 0.30$. The points are numerical calculations carried out with $D/2 = 1.0 \times 10^{-2}$, $b = 1.0 \times 10^{-4}$, plotted in dimensionless units.

points in Fig. 32 collapse into two points of the v_s axis which are in good agreement with Eq. (33) over a wide range of the geometrical parameters. Secondly, the depinning velocity for pure normal flow has been computed as a function of α , for the representative values $D/2 = 1.0 \times 10^{-2}$ cm, $b = 1.0 \times 10^{-4}$ cm. The results are given in Fig. 38. Finally, various $v_{s,\text{pin}}$, $v_{n,\text{pin}}$ pairs have been computed for the representative case $D/2 = 1.0 \times 10^{-2}$ cm, $b = 1.0 \times 10^{-4}$, and $\alpha = 0.30$, as shown in Fig. 37. It is clear from Figs. 32, 36, and 37 that Eq. (33) gives a very good fit to the computer experiments.

We conclude by mentioning two interesting additional results. If the normal fluid is taken to have the parabolic profile of Eq. (30), the numerical results differ by only a few percent from those obtained with uniform flow. Hence, the issue of what $\mathbf{v}_n(\mathbf{r})$ looks like does not appear

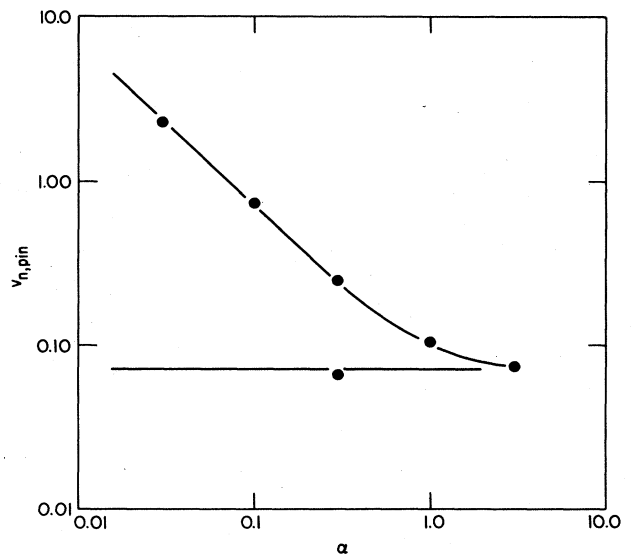


FIG. 38. Depinning velocity predicted by Eq. (33) for pure normal flow (top curve) and pure superflow (bottom curve) as a function of α , with $D/2 = 1.0 \times 10^{-2}$, $b = 1.0 \times 10^{-4}$. The points are numerically calculated values.

to be important for pinning phenomena. Also, it is found that if the two pinning sites are shifted so as not to be directly opposite each other, the depinning velocity is lowered.

V. DISCUSSION

It is a reasonable working hypothesis that flow phenomena involving quantized vortices in superfluid ^4He can largely be understood in terms of classical vortex dynamics, slightly modified to reflect the simpler properties of the quantized vortex. Since the nonlinear dynamics of three-dimensional vortices interacting with boundaries and with other vortices is not particularly easy to visualize, nor amenable to analytical treatment, the use of numerical simulation is essential, both to educate the intuition and to achieve quantitative predictions. In pursuing such a program, one finds it necessary to introduce certain straightforward ideas which have not previously been raised in the ^4He context. The present paper has aimed to clarify these basic ideas and to justify them as far as possible.

To be more specific, a recently introduced, successful theory of homogeneous superfluid turbulence⁴⁹ treated the dynamics of the vortex tangle in the local approximation, but added the at the time *ad hoc* idea that whenever two lines try to cross, they undergo a reconnection. The discussion of Sec. III B shows that the nonlocal interaction between two vortex lines generates a reconnection essentially identical to that assumed in the theory. To generalize the homogeneous turbulence theory to the case of flow through a channel, the notion was later introduced that a vortex line near a boundary will reconnect to the boundary.⁵⁰ The discussion of Sec. III A shows this idea to be correct. The channel flow theory, which applies only to the case of ideally smooth channel walls, predicts the existence of a critical velocity below which the turbulence cannot be self-sustaining. The calculations, however, showed a strong sensitivity to pinning, and, indeed, recent experiments^{44,45} have indicated that the initiation of superfluid turbulence involves initially pinned (remanent) vorticity in an essential way. The investigation of Sec. IV is a first step toward understanding these more complicated phenomena. There is, in fact, a suggestive qualitative similarity between the depinning velocities discussed here and the observed critical velocities for pure superflow and counterflow. Quantitatively, however, the observed critical velocities are about an order of magnitude greater than those predicted by Eq. (33), implying that they cannot be understood simply in terms of the depinning of an isolated vortex. The logical next step will be to consider the dynamics of an assembly of interacting pinned vortex lines, an interesting project which may cast further light on the nature of remanent vorticity and on the initiation of superfluid turbulence.

ACKNOWLEDGMENT

This work was supported in part by the National Science Foundation through Grant No. DMR-80-05385.

APPENDIX

The purpose of this section is to describe the methods by which the numerical computations are carried out. The discussion applies to the vortex-tangle calculations reported previously^{49,50} as well as to the calculations presented in this paper. The methods were developed heuristically, without reference to similar programs written by others and without much knowledge of the arcana of numerical analysis. There is no claim that they represent the state of the art either in sophistication or efficiency. The reliability of the codes was tested by comparing them against analytical results for the propagation of quantized vortex rings, and the rotation of vortex waves on a straight line. It was found that these properties can be calculated to very high accuracy if desired, and that accuracy on the order of a percent is obtainable with relatively modest computations ranging from one up to a hundred minutes of IBM 3081 CPU (central processing unit) time. In general, the main factor limiting the speed of the calculations is not the degradation of accuracy as the time steps are increased, but the sudden onset of numerical instabilities.

The configuration of vortices in a given problem is given by specifying a single string of points, indexed from $i=1$ to $i=i_{\text{max}}$. As many as 10000 points have been used in some of the vortex-tangle simulations. Associated with each point i are three spatial coordinates. Because of the frequent reconnections and interpolations necessary in some of the computer experiments, it is quite inconvenient to maintain sequential labeling of the points along each vortex. Instead, the label $i+$ of the point to which the line goes next and the label $i-$ of the point from which the line comes are also specified for each i . Reconnections and interpolations can then be effected by switching these pointers. In addition, each i carries a label which flags special points such as a point terminating on a pinning site, a special entry point on a closed vortex loop, and so on. This device chops the string of points into individual vortices and lets the program deal with the end points in whatever special way is required.

As the vortex configuration develops dynamically, it is necessary to add or remove points according to specific resolution requirements. For some problems, such as the vortex-tangle simulations, only a relatively narrow range of scales is of interest and it is sufficient to use the same resolution everywhere. In the kind of calculations done in this paper, however, it often proves advantageous to use a resolution criterion which varies along the vortex. For example, in the reconnection calculations of Sec. III A, points are continuously interpolated so that they are very close together ($l \sim \Delta/5$) in the reconnection cusp region, and much farther apart ($l \sim R/5$) far from the plane. The actual procedure used to interpolate between two adjacent points i and $i+$ is to find the mean vector curvature $\mathbf{s}'' = (\mathbf{s}_i'' + \mathbf{s}_{i+}'')/2$, and to place the new point on the midpoint of the arc generated by drawing a circle of radius $R = |\mathbf{s}''|^{-1}$ through the two points, the plane of the circle being defined by \mathbf{s}'' and $\mathbf{l} = \mathbf{s}_{i+} - \mathbf{s}_i$. This produces a smooth interpolation which is exact for points lying on a circular arc.

Generation of the vortex motion requires finding three kinds of contributions at every point: the locally self-induced motion $\beta s' \times s''$, the rest of the ideal-fluid motion consisting of the sum of nonlocal, boundary-generated, and applied fields, and the additional motion generated by friction [see Eqs. (7) and (11)]. To initiate a time step, the first task performed in the program is the evaluation of the nonlocal, boundary-generated, and applied fields, hereafter referred to simply as the nonlocal fields, to the extent that these are of interest. A straight-line element running from point j to $j +$ will contribute

$$\Delta v_{nl}^j(s_i) = \frac{\kappa}{2\pi(4ac - b^2)} \left[\frac{2c + b}{(a + b + c)^{1/2}} - \frac{b}{a^{1/2}} \right] \times (s_j - s_i) \times (s_{j+} - s_j) \quad (\text{A1})$$

to the velocity at point i , where $a = |s_j - s_i|^2$, $b = 2(s_j - s_i) \cdot (s_{j+} - s_j)$, and $c = |s_{j+} - s_j|^2$. This expression is summed over all real, image, or continued vortex segments not contiguous to i . If pinning site boundary corrections are to be considered, the gradient of the series given in Eqs. (18) or (19) (as appropriate) must be summed for each⁵¹ line element $s_{j+} - s_j$ and added to $v_{nl}(s_i)$. The applied field $v_{s,a}(s_i)$ is then added to complete the first task. Naturally, this sequence, which must be carried out for every i , is quite time consuming. Accurate nonlocal calculations are therefore practical only for relatively simple vortex configurations such as those considered in the present paper. The vortex-tangle calculations reported in Refs. 49 and 50 were carried out in the local approximation using a reconnection ansatz. If a nonlocal calculation is really necessary, large amounts of computer time can usually be saved at a modest cost in accuracy by (a) counting nonlocal contributions only from within some vicinity of the point of interest, and (b) evaluating the nonlocal terms only every few time steps.

The second task performed in the program is to deal with the local term $\beta s' \times s''$. The quantities s'_i and s''_i are evaluated by passing a circle through $i -$, i , and $i +$. One obtains

$$s'_i = d_i^+ l_+ + d_i^- l_- , \quad (\text{A2})$$

$$s''_i = c_i^+ l_+ - c_i^- l_- , \quad (\text{A3})$$

where

$$d_i^\pm = \frac{l_\mp^2}{|l_+ l_-^2 + l_- l_+^2|} , \quad (\text{A4})$$

$$c_i^\pm = \frac{a_\pm}{|a_+ l_+ - a_- l_-|^2} , \quad (\text{A5})$$

with

$$a_\pm = \frac{1}{2} \frac{l_+^2 l_-^2 + l_\mp^2 l_+ \cdot l_-}{l_+^2 l_-^2 - (l_+ \cdot l_-)^2} . \quad (\text{A6})$$

Here, $l_+ = s_{i+} - s_i$ and $l_- = s_i - s_{i-}$. The explicit form of the difference equation for the ideal-fluid motion now takes the form

$$\Delta s_i = -\gamma_i (s_{i+} - s_i) \times (s_i - s_{i-}) , \quad (\text{A7})$$

where

$$\gamma_i = \beta_i (d_i^+ c_i^- + d_i^- c_i^+) \Delta t . \quad (\text{A8})$$

Here, β_i has the value $(\kappa/4\pi) \ln[2(l_+ l_-)^{1/2}/e^{1/4} a_0]$ for a fully nonlocal calculation, the value $(\kappa/4\pi) \ln(\langle R \rangle/a_0)$ for a calculation in the local approximation, and the value 1 when working in dimensionless units.

The explicit forward integration of Eq. (A7) is numerically unstable. A distortion with a wavelength of twice the point spacing should, according to Eq. (15), undergo the retrograde rotation illustrated in Fig. 39. The naive difference equation, however, generates the linear displacements shown and therefore causes the amplitude of the wave to grow at each step. To handle this difficulty, a modified hopscotch algorithm^{52,53} is adopted. First, s_i is replaced by its forward value $s_i + \Delta s_i$ on the right-hand side of Eq. (A7) at every other point of the vortex, leaving the neighboring s_{i-} and s_{i+} points at their present value (Fig. 40). The result is an implicit equation which has the solution

$$\Delta s_i = \frac{\mathbf{A}_2 - \mathbf{A}_1 \times \mathbf{A}_2}{1 + A_1^2} , \quad (\text{A9})$$

where

$$\mathbf{A}_1 = \gamma_i (s_{i+} - s_i) , \quad (\text{A10})$$

$$\mathbf{A}_2 = -\gamma_i (s_i - s_{i-}) \times (s_i - s_{i-}) . \quad (\text{A11})$$

The set of points left behind is then moved forward in an explicit step, using the now-known forward values of the neighboring points (Fig. 40). The initial values of γ_i are used for both operations. On the next time step, the order in which the points are taken is switched. In practice, it was found that the accuracy and stability of the algorithm was improved by dropping A_1^2 from the denominator of Eq. (A9). To obtain the total ideal-fluid displacement Δs_i , the nonlocal term $v_{nl}(s_i) \Delta t$ can either be added ex-

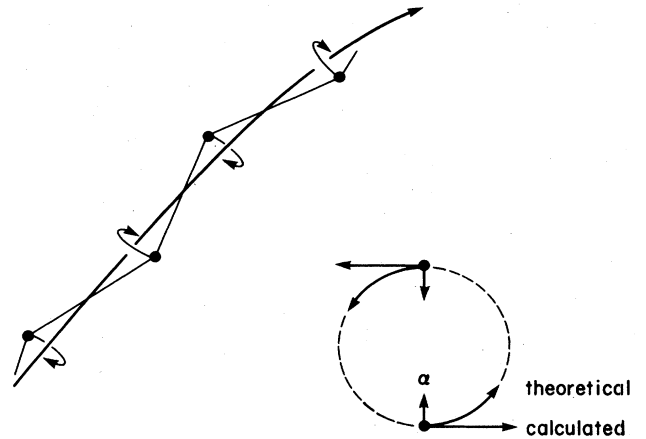


FIG. 39. Numerical instability wave on a vortex line. The end-on view at bottom right shows the amplification of the instability in an explicit calculation. The friction term α opposes this tendency.

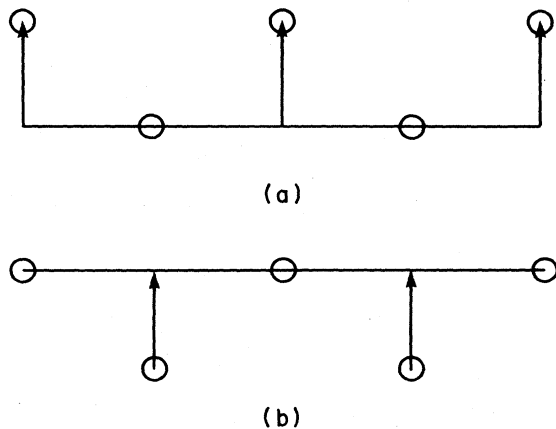


FIG. 40. Hopsotch sequence. (a) implicit step using forward values of points to be evaluated and present values of neighboring points; (b) explicit step using present values of remaining points and forward values of their neighbors.

plicitly, or taken into the explicit-implicit loop just described. The latter is usually more advantageous since in most situations the self-induced motion and \mathbf{v}_{nl} tend to cancel.

The final task is to take account of the frictional motion. To do this, Δs_i computed in the previous two steps is converted into a velocity $\dot{s}_0(s_i) = \Delta s_i / \Delta t$ and an explicit forward step is taken using Eq. (11), where s_i' is evaluated according to Eq. (A2).

The procedure described above generates the real dynamical behavior of the vortex configuration. For problems such as vortex pinning, where one is interested in computing some final stationary state involving a wide range of scales and a varying resolution criterion, it is much faster to use a time step which varies according to length of the line elements along the vortex. In this way the vortex can be made to relax quickly to its final state, but in a manner which no longer represents its real motion.

We now turn to the question of how well these programs actually work. This will be discussed in terms of a few illustrative examples. Let us first consider a vortex ring in the absence of friction. It is found that as the point spacing and time steps are made small, the propagation velocity of the ring reaches a well-defined value slightly exceeding that predicted by Eq. (2). This offset, interestingly enough, arises from the fact that the nonlocal contribution is evaluated by summing over straightline elements according to Eq. (A1). If the local line element is held fixed in length, and the spacing of the rest of the points is decreased, the nonlocal term [Eq. (3)] is approached exactly. If, however, the local line length element is also decreased in length, the increasing relative accuracy of the nonlocal term must compete with the fact that it diverges as the local element goes to zero. The outcome of this competition is a draw which adds a small constant to the logarithm, giving

$$\dot{s}(\text{ring}) = \frac{\kappa}{4\pi R} \hat{\mathbf{z}} \left[\ln \left[\frac{8R}{e^{1/4} a_0} \right] + 0.0768 \right]. \quad (\text{A12})$$

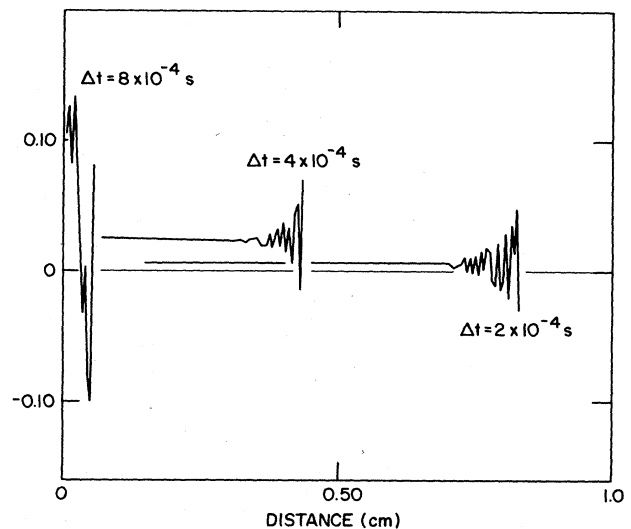


FIG. 41. Computed propagation velocity of a vortex ring of radius 1.0×10^{-2} cm, in the absence of friction. Shown is the fractional deviation of the velocity from Eq. (A12) as a function of distance traveled, for various time steps. If a friction term $\alpha = 0.10$ is added, the propagation becomes completely stable for all three Δt s.

Although such a small correction is insignificant to the physics, it is important in judging the accuracy of the algorithm to remember that it is structured to approximate Eq. (A12).

The major characteristics of the program are displayed in Fig. 41. Looking at the computed propagation of a vortex ring, one observes a constant deviation from the analytical result of Eq. (A12), and the eventual development of an explosive instability. As the time step is decreased, the deviation goes rapidly to zero, and the instability is pushed out to longer times. Using reasonable time steps, it is not difficult to propagate the vortex ring to a distance of a hundred radii with essentially perfect accuracy.

Figure 41 shows that the hopsotch algorithm does not eliminate the instability entirely in the absence of friction. The error wave shown in Fig. 39 still grows, albeit very much more slowly. We now recall from Sec. IID that the dissipation term will cause small scale deformations to decay preferentially. That is, the error wave in Fig. 39 will decrease in amplitude as it rotates, provided the frictional term outweighs the error growth rate. Indeed, if α is nonzero, one can always find a Δt below which the calculation becomes absolutely stable. If this value is exceeded, the instability rapidly makes its appearance. When the calculations of Fig. 41 are repeated⁵⁴ with a dissipation of $\alpha = 0.10$, the calculation is absolutely stable for $\Delta t = 8 \times 10^{-4}$ s and smaller, and unstable for $\Delta t = 16 \times 10^{-4}$ s. The deviation of the calculated velocity from Eq. (A12) is 11.8% when $\Delta t = 8 \times 10^{-4}$ s, 2.5% when $\Delta t = 4 \times 10^{-4}$ s, and 0.6% when $\Delta t = 2 \times 10^{-4}$ s. This is representative of the behavior found at all scales and point spacings: The errors are always of order 10% just below the stability limit, and rapidly become insignifi-

cant as Δt is reduced further.

The stability limit itself has been studied numerically, and can be described roughly by

$$\Delta t \sim \gamma l^{1.75} R^{0.4} / \beta, \quad (\text{A13})$$

where l is the smallest point spacing. Here, $\gamma \sim 1$ for $\alpha = 0.10$ and decreases slowly as α becomes smaller. In most calculations, the program uses Eq. (A13), with a suitably chosen γ , to continually adjust its own time steps and stay well within the stability limit. It is easy to see from Eq. (A13) that the number of time steps required to generate some characteristic motion, such as propagation of the ring through a distance equal to one radius, is almost independent of the ring size. Merely changing the scale of the problem does not affect the cost of the calculation. It is equally obvious, however, that improving the

resolution (decreasing l) for a given calculation is very expensive, the cost increasing as $l^{-2.75}$.

Many other studies of the program's performance have been done. To quote one final example, we have investigated the behavior of a sinusoidal wave of very low amplitude on a straight line. Theory shows^{21,55} that the sine wave undergoes a retrograde rotation with an angular frequency,

$$\omega = \frac{\kappa k^2}{4\pi} \left[\ln \left[\frac{2}{ka_0} \right] - \gamma + \frac{1}{4} \right], \quad (\text{A14})$$

where k is the wave number of the distortion and γ is Euler's constant. Even with a relatively crude resolution $kl \sim 0.25$, the calculations match Eq. (A14) to within 0.1%, and are stable for many revolutions, provided Δt is chosen properly.

- ¹R. P. Feynman, in *Progress in Low Temperature Physics*, edited by C. J. Gorter (North-Holland, Amsterdam, 1955), Vol. I, p. 15.
- ²H. E. Hall and W. F. Vinen, Proc. R. Soc. London, Ser. A **238**, 204 (1956); **238**, 215 (1956).
- ³E. B. Sonin, Zh. Eksp. Teor. Fiz. **70**, 1970 (1976) [Sov. Phys.—JETP **43**, 1027 (1976)].
- ⁴M. R. Williams and A. L. Fetter, Phys. Rev. B **16**, 4846 (1977).
- ⁵L. J. Campbell and R. M. Ziff, Phys. Rev. B **20**, 1886 (1979).
- ⁶E. J. Yarmchuk and R. E. Packard, J. Low Temp. Phys. **46**, 479 (1982).
- ⁷C. D. Andereck and W. I. Glaberson, J. Low Temp. Phys. **48**, 257 (1982).
- ⁸G. W. Rayfield and F. Reif, Phys. Rev. **136**, A1194 (1964).
- ⁹W. I. Glaberson and M. Steingart, Phys. Rev. Lett. **26**, 1423 (1971).
- ¹⁰For a recent review of this subject, see J. T. Tough, in *Progress in Low Temperature Physics*, edited by D. F. Brewer (North-Holland, Amsterdam, 1982), Vol. VIII, p. 133.
- ¹¹W. F. Vinen, Proc. R. Soc. London, Ser. A **242**, 493 (1957).
- ¹²K. W. Schwarz, Phys. Rev. B **18**, 245 (1978).
- ¹³J. S. Langer and J. D. Reppy, in *Progress in Low Temperature Physics*, edited by C. J. Gorter (North-Holland, Amsterdam, 1970), Vol. VI, p. 1.
- ¹⁴R. J. Donnelly and P. H. Roberts, Proc. R. Soc. London, Ser. A **312**, 519 (1969).
- ¹⁵K. W. Schwarz, Phys. Rev. Lett. **47**, 251 (1981).
- ¹⁶K. W. Schwarz, Physica **108B**, 1121 (1981).
- ¹⁷K. W. Schwarz, in *Proceedings of the 75th Jubilee Conference on Helium-4*, edited by J. G. M. Armitage (World Scientific, Singapore, 1983), p. 60.
- ¹⁸E. D. Siggia (unpublished).
- ¹⁹W. F. Vinen, in *Progress in Low Temperature Physics*, edited by C. J. Gorter (North-Holland, Amsterdam, 1961), Vol. III, p. 1.
- ²⁰W. F. Vinen, in *Quantum Fluids*, edited by D. F. Brewer (North-Holland, Amsterdam, 1966), p. 74.
- ²¹A. L. Fetter, in *The Physics of Liquid and Solid Helium*, edited by K. H. Benneman and J. B. Ketterson (Wiley, New York, 1974).
- ²²C. F. Barenghi, R. J. Donnelly, and W. F. Vinen, J. Low Temp. Phys. **52**, 189 (1983).
- ²³A. J. Hillel and W. F. Vinen (unpublished).
- ²⁴H. Lamb, *Hydrodynamics* (Dover, New York, 1945), Chap. VII.
- ²⁵A. Leonard, J. Comp. Phys. **37**, 289 (1980).
- ²⁶P. G. Saffman, Stud. Appl. Math. **49**, 371 (1970).
- ²⁷Since the filaments can stretch and shrink, this parameter must be redefined at every instant. See Ref. 12 for a more general procedure.
- ²⁸Only rigid, stationary boundaries will be considered. The extension to moving boundaries is obvious.
- ²⁹The use of $\alpha = \rho_n B / 2\rho$ and $\alpha' = \rho_n B' / 2\rho$ in place of the conventional Hall-Vinen parameters B and B' simplifies the equations at no cost to their information content. See Ref. 2.
- ³⁰Different notation is used for the superfluid and normal-fluid velocities in order to emphasize the unfortunately often overlooked fact that, whereas v_s is meaningful down to the angstrom scale, v_n represents a coarse-grain average over the excitation gas, and hence is meaningful only down to the scale of the excitation mean free path.
- ³¹F. R. Hama, Phys. Fluids **6**, 526 (1963).
- ³²R. J. Arms and F. R. Hama, Phys. Fluids **8**, 553 (1965).
- ³³Additional factors can be expected to enter near the λ point, where thermal fluctuations and other complications become important, and at low temperatures ($\alpha \rightarrow 0$), where such classical ideas as vortex stretching may be relevant.
- ³⁴K. W. Schwarz, Phys. Rev. A **10**, 2306 (1974).
- ³⁵The finite-core structure is not taken into account in these calculations.
- ³⁶By this we mean the boundary field arising from the sphere. The plane-boundary condition is automatically satisfied by extending the vortex symmetrically as shown in Fig. 20.
- ³⁷Alternatively one can imagine the vortex filament as undergoing self-induced motion because of its curvature, $v_{s,a}$ then being replaced by $(\kappa/4\pi R) \ln(cR/a_0)$.
- ³⁸H. E. Hall, Philos. Mag. Suppl. **9**, 89 (1960).
- ³⁹E. L. Andronikashvili and D. S. Tsakadze, J. Exptl. Theoret. Phys. (U.S.S.R.) **37**, 322 (1959) [Sov. Phys.—JETP **10**, 227 (1960)].
- ⁴⁰E. L. Andronikashvili, Yu. G. Mamaladze, S. G. Matinyan, and D. S. Tsakadze, Usp. Fiz. Nauk. **73**, 3 (1961) [Sov. Phys.—Usp. **4**, 1 (1961)].
- ⁴¹E. J. Yarmchuck and W. I. Glaberson, Phys. Rev. Lett. **41**, 564 (1978); E. J. Yarmchuck and W. I. Glaberson, J. Low Temp. Phys. **36**, 381 (1979).
- ⁴²S. G. Hegde and W. I. Glaberson, Phys. Rev. Lett. **45**, 190 (1980).

- ⁴³W. I. Glaberson and R. J. Donnelly, *Phys. Rev.* **141**, 208 (1966).
- ⁴⁴M. L. Baehr, L. B. Opatowsky, and J. T. Tough, *Phys. Rev. Lett.* **51**, 2295 (1983).
- ⁴⁵D. D. Awschalom and K. W. Schwarz, *Phys. Rev. Lett.* **52**, 49 (1984).
- ⁴⁶This is slightly different from the convention used in Ref. 15. To save computer time, most calculations were carried out for this symmetrical case.
- ⁴⁷As usual, the second friction coefficient α' has been neglected in these calculations.
- ⁴⁸For large pinning sites the agreement is not quite as good because the flow field corrections near the pinning site become significant.
- ⁴⁹K. W. Schwarz, *Phys. Rev. Lett.* **49**, 283 (1982).
- ⁵⁰K. W. Schwarz, *Phys. Rev. Lett.* **50**, 364 (1983).
- ⁵¹Except for the points terminating on the pinning sites, as noted earlier.
- ⁵²P. Gordon, *J. Soc. Ind. Appl. Math.* **13**, 667 (1965).
- ⁵³A. R. Gourlay and G. R. McGuire, *J. Inst. Math. Its Appl.* **7**, 216 (1971).
- ⁵⁴A comoving normal fluid is added to keep the ring from decaying.
- ⁵⁵W. Thompson (Lord Kelvin), *Philos Mag.* **10**, 155 (1880). This expression can easily be derived from Eq. (5) by explicit calculation.